This document was prepared for the ETI by third parties under contract to the ETI. The ETI is making these documents and data available to the public to inform the debate on low carbon energy innovation and deployment.

Programme Area: Marine

Project: PerAWAT

Title: Report on Nonlinear Analysis of a Single Controlled Device in Irregular Seas, Report on Nonlinear Analysis of Controlled Arrays in Irregular Seas

Abstract:

This report concerns the fully nonlinear simulations of the behaviour and performance of a single axisymmetric device and small arrays of axisymmetric devices, respectively, in irregular waves subject to linear and nonlinear power take-off (PTO) forces with different control strategies. The key objectives of the work were to simulate irregular waves effectively, to model the operation of axisymmetric devices subject to both linear and nonlinear PTO forces and to investigate the effect of device and array control strategies. The report outlines how these objectives have been met and any issues arising from their completion. An investigation into the importance of nonlinear contributions to free-surface elevation and also to the device response and power take-off by simulating a particular sea state with increasing significant wave height values is also reported. The different responses of the devices in irregular waves subject to linear and nonlinear PTO forces are also analysed and reported here.

Context:

The Performance Assessment of Wave and Tidal Array Systems (PerAWaT) project, launched in October 2009 with £8m of ETI investment. The project delivered validated, commercial software tools capable of significantly reducing the levels of uncertainty associated with predicting the energy yield of major wave and tidal stream energy arrays. It also produced information that will help reduce commercial risk of future large scale wave and tidal array developments.

Energy Technologies Institute

PerAWaT

WG1 WP1 D11: Report on nonlinear analysis of a single controlled device in irregular seas

WG1 WP1 D12: Report on nonlinear analysis of controlled arrays in irregular seas

Author: C. Fitzgerald

Checked by: P. H. Taylor and R. Eatock Taylor

Date: 21st February 2013

Version 1.0

CONTEXT

This report is comprised of deliverable WG1 WP1 D11 and WG1 WP1 D12 which concern the fully nonlinear simulations of the behaviour and performance of a single axisymmetric device and small arrays of axisymmetric devices, respectively, in irregular wave subject to linear and nonlinear PTO forces with different control strategies. Prior to these two deliverables, the uncontrolled and controlled response and power capture of axisymmetric devices have been simulated in regular incident waves only. Furthermore, the axisymmetric device geometry used thus far in deliverables WG1 WP1 D9 (uncontrolled response) and WG1 WP1 D10 (power capture subject to control and power take-off forces) has been that of a truncated cylinder. In this deliverable, the axisymmetric device is a vertical cylinder with a hemispherical end which is the geometry used in the experimental tests reported in WG2 WP2 D5. Therefore, these two deliverables involve important progress towards future deliverables (WG1 WP1 D13) involving validation of the fully nonlinear code OXPOT with experimental test results.

The key objectives of the deliverables were to simulate irregular waves effectively, to model the operation of axisymmetric devices subject to both linear and nonlinear PTO forces and to investigate the effect of device and array control strategies. This report outlines how these objectives have been met and any issues arising from the completion of these objectives. An investigation into the importance of nonlinear contributions to free-surface elevation and also to the device response and power take-off by simulating a particular sea state with increasing significant wave height values is also reported. The different responses of the devices in irregular waves subject to linear and nonlinear PTO forces are also analysed and reported here.

TABLE OF CONTENTS

1 INTRODUCTION

1.1 Scope of this document

To investigate the operation of wave energy devices in real seas, an implementation of irregular wave generation in the fully nonlinear potential flow solver OXPOT is utilised. The combination of this irregular wave generation implementation with the introduction of power take-off forces to the equation of motion, as implemented for a previous deliverable (WG1 WP1 D10), allows the simulation of the performance of a single device and an array of devices in a random sea. This report contains the results and analysis for the performance of a single axisymmetric device and an array of devices in irregular waves subject to linear and nonlinear PTO forces and different control strategies.

This report comprises three main sections. A brief overview of the random nature of real ocean waves and, in particular, the weakly nonlinear description of the irregular waves in moderate seas is provided in section 2. In section 3, the results of single device simulations of unidirectional irregular wave interactions involving a device subject to linear and nonlinear PTO forces and restoring force terms are analysed and discussed. Thereafter, the results of the simulation of square array operation in irregular waves are presented in section 4.

Section 2 contains an overview of the random nature of real ocean waves and a description of methods to obtain numerical realisations of the irregular seas from the sea state energy spectrum. A discussion of the random nature of real ocean waves and different methods for representing this randomness is included this section. For simulations where the most important quantity is the mean power absorbed, the random nature of the sea does not need to be represented in full and using deterministic values for the wave component amplitudes in combination with randomly selected phases is acceptable. If the statistical variation of the power absorbed is of interest then this would not be the case and another better wave representation is needed (as noted by (Tucker, et al., 1984) in relation to the free-surface elevation in simulated wave records). The irregular wave generation approach, in particular the method to compute the amplitude (deterministic) and phase (random) of the individual wave components, is then described in full. Furthermore, the decomposition of the incident waves into N Fourier components with frequency increment df determined from the desired rrepeat period is also briefly summarised from WG1 WP1 D1B. Thereafter, the results of some simulations of irregular wave propagation in a narrow wave flume for different target energy spectra (corresponding to the unidirectional sea states from the experimental work in WG2 WP2 D5) are presented. The approach to wave generation in these simulations is repeated later for the interaction simulations.

The interaction of a single rounded vertical truncated cylinder with irregular incident waves is considered in section 3. This rounded vertical cylinder geometry was used by QUB in the experimental investigations reported in WG2 WP2 D5. Future deliverables will require the simulation of the experimental work and so it was decided to simulate the response of this particular structure

to incident waves and to simulate the power capture when subject to power take-off (PTO) forces. Therefore, section 3 contains analysis of the heave displacement response of the rounded truncated cylinder (or 'device') in different irregular seas and subject to both linear and nonlinear PTO damping forces. A brief investigation of the relevance of the regular-wave optimal power absorption conditions (for linear PTO damping and restoring coefficients) to power absorption in irregular sea states is conducted. The importance of nonlinearity in a particular sea state is examined in some detail in this section also. The experimental sea states are essentially linear in nature and so to observe the effect of hydrodynamic nonlinearity on the device response or power absorption it is necessary to increase the significant wave height of the sea state incrementally. The device response is then considered during the same large event in each sea state. Some clear nonlinearity is evident in the free-surface elevation during the large event and leads to small second order contributions to device response.

The analysis of array interactions consists of two separate investigations. In the first, the behaviour of a long line of units aligned perpendicular to the direction of wave incidence is analysed for different device spacing. The long line of units is approximated by an infinite line of units which corresponds, through symmetry in the side walls, to a single device in a narrow wave flume with perfect wave reflection at the walls. The long line of devices is simulated for device spacings of three diameters and five diameters, and compared to a single device operating in effective isolation – this analysis is in section 3. In section 4, the simulation results for the operation of a square array of four devices in incident irregular waves with different underlying energy spectra are presented and briefly discussed. The power take-off forces considered are the linear damping and Coulomb damping force. A comparison of the response and performance of a device in isolation to the same device in a square array is also presented. Mean power capture values are computed for the devices in the array in different sea states and for different PTO damping forces. Some conclusions are then outlined in section 5.

1.2 WG1 WP1 D11 + D12 acceptance criteria

The acceptance criteria for WG1 WP D11 are:

"The report will summarise the methodology used and present the results: i.e. effect of different control strategies on the performance of single axisymmetric devices in irregular waves; and the effect of different linear and nonlinear PTOs. In so far as it is possible prior to validation, findings will be discussed and applications and limitations of this approach will be described including any lessons-learned on methodology."

and for and WG1 WP1 D12 are:

"The report will summarise the methodology used and present the results: i.e. the effect of different array control strategies on the performance/behaviour of arrays in irregular waves. Assessment and Report will as a minimum include arrays of four units and a long line of units."

The areas of the report addressing these criteria are sections 3 and 4. Results for the simulations of the fully nonlinear response and performance of a single axisymmetric device in irregular waves are presented in section 3 and include investigations into the effects of linear and nonlinear PTOs and the effects of device control through the PTO force. In addition, section 3 contains an analysis of the

performance of a long line of units subject to a linear PTO with two different device-spacings and different array control strategies through the variation in PTO settings. The results for simulations of the performance of arrays of four devices in irregular seas subject to linear and nonlinear PTO forces are presented and discussed in section 4.

2 IRREGULAR WAVE GENERATION

2.1 Sea state parameterisation

The waves encountered in real sea states are described as 'irregular' in order to distinguish them from the 'regular' monochromatic waves which are often considered in preliminary theoretical investigations of hydrodynamic interactions. Irregular sea states can be modelled approximately as comprising a superposition of random waves of different frequencies, i.e. a superposition of regular wave components. In a linear description, each wave component will provide a single contribution at a single frequency to the total sea state. Such a description is accurate only in small seas where nonlinearity is negligible. For moderate seas, the effect of nonlinear wave-wave interactions must be included using a Stokes' expansion approach and at second order this results in additional wave components at sum and difference frequencies for each pair of waves. In effect, the linear solution is perturbed by a small but significant second order term. For strongly nonlinear waves, this perturbation approach may not be suitable for analysis; however, for the sea states considered by QUB in the experimental tests described in WG2 WP2 D5, and which comprise the cross-validation cases for the other numerical models in WG1, this perturbation approach should be sufficient. The other numerical analyses in WG1 are all conducted in the context of linear theory. So it is necessary to include here, albeit limited in scope, a theoretical discussion of the nonlinear contributions prior to an analysis of the results of the nonlinear solver.

To simulate the controlled motion of single isolated axisymmetric devices and arrays of axisymmetric devices in an irregular sea, it is first necessary to generate a random wave-train from the sea's target energy spectrum. The target spectra considered here are deterministic expressions modelling typical wave records for fully-developed seas (Pierson-Moskowitz) and developing seas (JONSWAP). For seas where nonlinearity is very weak or negligible such spectra provide a good representation of the actual distribution of energy over the frequency range for an infinitely long wave record. However, for mild-to-moderate seas, these target wave spectra represent the energy distribution of the fundamental linear waves but not the higher harmonics arising from nonlinear wave-wave interactions. For example, if measurements of the free-surface elevation at a point on the free surface of a moderately nonlinear sea were taken then the energy spectrum generated from these measurements will contain a secondary peak at twice the peak frequency due to a contribution of the super-harmonic. In fact, in some presentations of deterministic spectral expressions it is assumed that the expressions are only valid for $\omega < 2\omega_0$ where $\omega_0$is the peak frequency. Nevertheless, to generate the desired sea states it is necessary to build from the linear representation and so initial computations involve the familiar deterministic expressions for the Pierson-Moskowitz (P-M) and JONSWAP spectra. Nonlinearity can be incorporated using the perturbation approach.

The incident polychromatic sea states considered in this deliverable are all unidirectional and are a subset of the set considered by QUB in the experimental tests described in WG2 WP2 D5.The target energy spectra of the sea-states we consider are characterised by three parameters: the significant

wave height H_s, a period parameter, and the peak enhancement factor γ. (Sea states can be characterised in terms of a variety of different period parameters defined in different ways, including the peak period, the energy period, the zero-crossing period and so on.) The particular period parameter chosen here is the energy period T_e defined as the ratio of the first negative moment of the spectrum $S(f)$ to the zeroth moment of the spectrum where a moment of the spectrum $S(f)$ is defined as

$$m_n = \int_0^\infty S(f) f^n df. \tag{1}$$

The peak enhancement factor γ is used to modify the Pierson-Moskowitz spectral expression

$$S(f) = \frac{A}{f^5} \exp\left(-\frac{B}{f^4}\right) \tag{2}$$

in order to account for the fact that the wave spectrum is never fully developed and continues to develop through nonlinear wave-wave interactions. The factor A is dependent upon H_s and T_e and B depends upon the period parameter only, as described in Appendix A of WG1 WP1 D1B. Therefore, the P-M spectrum can be expressed in terms of these two parameters only whereas a JONSWAP spectrum requires the peak enhancement factor γ in the following form,

$$S(f) = \frac{A}{f^5} \exp\left(-\frac{B}{f^4}\right) \gamma^{\exp\left(-\frac{(f-f_p)^2}{2\sigma^2 f_p^2}\right)} \tag{3}$$

where σ obeys

$$\sigma = \begin{cases} 0.07, & f < f_p \\ 0.09, & f > f_p \end{cases} \tag{4}$$

and γ is the parameter which determines how narrow is the peak of the spectrum. If $\gamma = 1$ then the spectrum reduces to the more broad-banded Pierson-Moskowitz spectrum.

The set of four sea states considered in this deliverable are shown in Table 1. The steepness parameter H_s/λ_e (where λ_e is the wavelength corresponding to the energy period) is largest for the sea-state with the smallest energy period and it can be expected that the influence of nonlinearity will be most pronounced in this case. The first three of these sea spectra are energetically quite similar and are compared in Figure 1. It is noticeable that sea state 1 has the narrowest peak due to the choice of peak enhancement factor $\gamma = 2$. Sea state 2 and sea state 3 both have broader spectra and are quite similar – sea state 3 which corresponds to the longest energy period has the largest peak. Sea state 4 is just sea state 3 with a larger (by a factor of two) significant wave height and has significantly more energy than the other spectra and hence is not shown.

Sea state	H_s (m)	$T_e(s)$	γ	H_s/λ_e
1	2	6.5	2	0.03
2	2	8	1	0.02
3	2	11.3	1	0.01
4	3	11.3	1	0.02

Table 1: The set of unidirectional sea states to be simulated in this deliverable. In some simulations $H_s = 4m$ was specified for SS4 because this value was suggested for numerical simulations whereas $H_s = 3m$ wa chosen for the experimental tests.

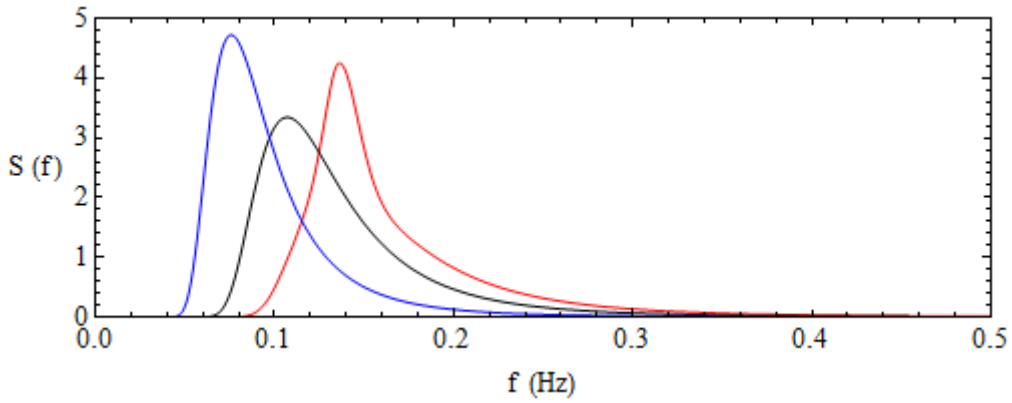

Figure 1: Plot of the target energy spectra of sea states 1 (red), 2 (black), 3 (blue) against frequency.

2.2 Irregular wave generation using a piston wavemaker

To generate a finite realisation of irregular waves corresponding to a prescribed sea state it is first necessary to understand the random nature and statistical properties of the sea surface. In order to do this, it is more straightforward to consider the linear representation only of the sea-state; the second-order contributions can be introduced as perturbations of the linear solution afterwards without a loss of accuracy provided the sea states are not extremely nonlinear. From a statistical perspective the sea surface is assumed to be a Gaussian process and is modelled as a linear superposition of wave components of different frequencies so the free-surface elevation can be written as

$$\zeta(x,t) = \sum_{n=1}^{N} c_n \cos(k_n x - \omega_n t + \varphi_n) \tag{5}$$

where k_n, ω_n and φ_n are the wavenumber, angular frequency and phase of each wave component and N is the number of wave components. The random nature of the sea state is included through

the amplitude $c_n$and phase φ_n of each wave component. Each measured wave record from a sea state over a given time interval will have a different energy spectrum due to the finite nature of a wave record and the Gaussian properties of the sea. The measured spectrum of the individual record/realisation is subject to a large sampling variance due to the stochastic nature of the surface but when averaged the spectra over different records will converge to the underlying spectrum $S(f)$. (Tucker, et al., 1984) demonstrated that the commonly used numerical simulation method, which involves the free-surface elevation expression (5) in conjunction with the deterministic amplitudes

$$c_n = \sqrt{2S(f_n)\Delta f_n} \tag{6}$$

obtained from the target energy density spectrum and with the stochastic nature of the sea included by choosing random phases ϕ_n from a uniform distribution on $(0,2\pi)$, does not model the random nature of the sea surface fully except in the limit $N \to \infty$. This is because the numerical realisations will always produce the desired spectrum $S(f)$ and in the process some of the randomness is lost. To model the true random nature of the sea-surface for a small finite number N of wave components it is necessary to express the sea-surface in an equivalent form to (5) as

$$\zeta(x,t) = \sum_{n=1}^{N} a_n \cos(k_n x - \omega_n t) + b_n \sin(k_n x - \omega_n t) \tag{7}$$

where a_n and b_n are independent normally distributed random variables with a common variance $\sigma_n^2 = S(f_n)\Delta f_n$ where Δf_n is the frequency increment. In practice, as noted in section 4.1.3 of WG1 WP1 D2, if the number N of wave components is sufficiently large then the difference between the representations in terms of the wave statistics is negligible. In the simulations conducted here, N is generally quite small and hence it is worth noting the restrictions of using the deterministic wave amplitude scheme.

Nevertheless, for the purposes of our investigations where the average value of the power absorbed is the important quantity then the quasi-deterministic representation is sufficient – we are not interested in sampling variability of the mean power capture for a given sea state. That is, we do not measure the power capture in different samples (realisations) of the same sea state spectrum. Therefore, we will not be able to estimate statistical variance or sampling variability of the power capture using this approach – the only output from the simulations of a given sea state energy spectrum will be the mean power absorbed. For a given target wave energy spectrum it is necessary to specify the number of wave components used to represent the sea state and to compute their amplitudes using equation (6) and to choose the phases randomly. If the frequency increment Δf is constant then the incident waves $\zeta(x,t)$ at a given location x will repeat after a time $T_r = 1/\Delta f$. In the simulations that follow[1], the frequency increment df was chosen to yield a certain repeat period T_r and the spectrum was discretised accordingly. For the spectrum associated with SS3, the repeat period was chosen to be $200s$ and hence the frequency increment equal to $0.005Hz$. (This is on the lower limits of an acceptable repeat period for computing mean power capture but is necessitated

[1] In some of the simulations required for comparison with the spectral wave model (SPECWEC) the wave component frequencies were already prescribed.

by the long computational times required for a fully nonlinear potential flow simulation.) The wave amplitudes were then obtained on the interval $(8f, 80f) = (0.04Hz, 0.4Hz)$ at each frequency increment. The same discretisation was used for the energy spectrum of sea-state 2. It should be noted that a repeat period of $200s$ corresponds to almost 18 energy periods for SS3 and 25 energy periods for sea state 2. In general, the longer the repeat period the better for obtaining average values with as little statistical variation as possible. The discretised target energy spectra with comparable total energy are illustrated in Figure 2.

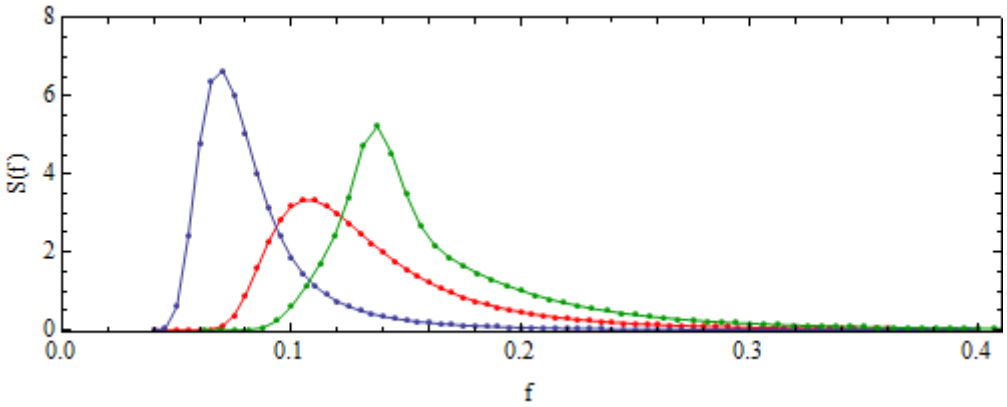

Figure 2: The discretisation of the JONSWAP energy spectra for sea state 1 (green), sea state 2 (red) and sea state 3 (blue).

It is useful to consider a sample wave generation simulation to illustrate some of the issues that can arise while generating irregular waves using OXPOT. For this purpose, a realisation of sea state 1 (SS1) is considered. For this sea state, the energy period is $T_e = 6.5s$, the significant wave height is $H_s = 2.0m$ and the waves propagate in water of depth $h = 50m$. The frequencies of the wave components were chosen so that the repeat period has the value $T_r = 160s$, that is, $df = 0.00625Hz$. Over 60 components were chosen to discretise the spectrum between $f_0 = 0.0625Hz$ and $f_1 = 0.45Hz$ and an illustration of the discretisation is shown in Figure 2. The set of wave amplitudes were determined by substituting the values of the spectra at the chosen set of discrete frequencies $S(f_n)$ into equation (6). Thereafter, the phases of the components were selected at random from a uniform distribution. In order to obtain the wavemaker amplitudes for the piston wavemaker implementation in OXPOT, the Biésel transfer function

$$T(k,h) = 2\tanh kh \sinh 2kh \,/(2kh + \sinh 2kh) \tag{8}$$

was used to scale the amplitudes. Therefore, as input to OXPOT we have a set of frequencies $\{f_n\colon\ n = 1, N\}$, a set of wavemaker amplitudes $\{c_n/T(k_n,h)\colon\ n = 1, N\}$ and a set of phases $\{\varphi_n\colon\ n = 1, N\}$ which specify the linear incident wave-field.

2.2.1 OXPOT simulations of wave generation

In order to simulate the generation and propagation of the irregular waves in OXPOT it is necessary to discretise the computational domain with sufficient fineness so that it can resolve a large range of frequencies. In some respects, this is no different to the regular wave simulations in deliverables D9

and D10 where as a minimum it was necessary to specify the mesh resolution so that (at least) the kinematics of the first and second order wave harmonics were captured. However, with irregular waves of relatively long repeat periods it is also necessary to specify a mesh which does not yield unnecessarily long computational times. Therefore, although the following mesh specification may seem rather coarse it is specified with the aim that it should be possible to use it in a simulation involving a floating cylinder or array of cylinders over a reasonable number (twenty five or more) of energy periods.

All OXPOT specifications are in non-dimensional terms so the lengths are all, at full scale, multiples of the water depth h. With this in mind it is useful to mention that the energy (peak) wavelength λ_e (λ_p) of the sea state, i.e. the wavelength corresponding to the energy (peak) period T_e (T_p), is approximately equal to $1.32h$ ($1.68h$). The domain is specified to have a length of $L_D = 8.0$ with the wavemaker positioned at $x = -4.8$ so that a cylinder centred on $x = 0$ will be almost three peak wavelengths from the wavemaker. The triangular free-surface elements are chosen to have a side of $\Delta x = 0.08$ so that there are 20 elements per peak-wavelength, 16 per energy wavelength and 10 elements per second-order sum bound wavelength. Given that each element has 6 nodes, this was considered sufficient to describe second order wave propagation. In terms of time-stepping, the increments were specified to be $\Delta t = T_e/40$ and so a simulation of a repeat period $T_r \simeq 24.6\, T_e$ involves approximately 1000 time steps. In general, it is necessary to simulate at least a repeat period and a half to allow time for the incident wave to arrive at the origin and so the number of time-steps for wave-propagation and device-interaction simulations will be approximately 1500 in this case. Prior to the description of the isolated device simulations a table will be provided to summarise the computational mesh details; here we will describe the meshes in detail.

To present the results in a meaningful way it is useful to compare the OXPOT results with the linear prediction based on equation (5). A comparison of the free-surface elevation as computed by OXPOT at a point on the free surface a single wavelength from the wavemaker to the linear prediction is shown in Figure 3. The agreement is quite good although quite a few of the peak amplitudes are not predicted correctly. There are a few possible reasons for this. Firstly, in the OXPOT simulations the high frequency waves may not be resolved fully and the cumulative effect is a reduction in the peak amplitudes. Secondly, the damping zone at the far end of the domain is effective at absorbing high frequency waves but may not be as effective with the long wave components so there may be some contamination by reflected long waves. Lastly, some of the energy introduced to the system by the linear wavemaker may be redistributed into second order wave components thus altering the linear system dynamics.

In terms of second order contributions, it is possible to separate the odd and even harmonics by running two simulations with the (first order) wavemaker signals in anti-phase. By taking the average of the difference and sum of the free-surface elevations it is possible to extract the odd and even harmonics dominated by the first and second order components respectively (see WG1 WP1 D9 for more details). The second order contribution relative to the first order contribution is shown in Figure 4 where it is clear that the second order wave amplitudes are relatively small. Furthermore, comparing the linearised OXPOT signal to the linear theoretical prediction does not yield a visibly better agreement – the difference is quite small. In order to illustrate the contribution that second order waves can make to an irregular sea state it is necessary to compare two sea-states generated

with identical phases for the wave components but with one sea-state having larger wave amplitudes.

To this end, and with device interaction simulations in mind, we consider the incident sea state spectrum SS2 with the significant wave height $H_s = 2m$ and also when quadrupled to $H_s = 8m$. Although it would seem more logical to follow up the SS1 investigation with another simulation involving larger wave amplitudes, in the single-device in isolation simulations we consider sea-state 2 and the corresponding larger amplitude sea state and so it is useful to present the results of the wave propagation simulations for both these incident waves in the absence of the cylinders.

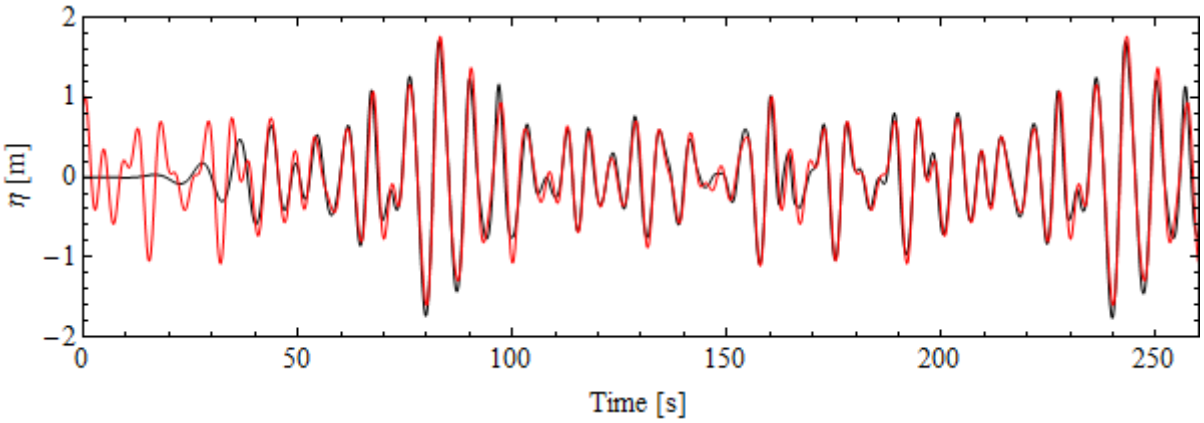

Figure 3: Free surface elevation at a point on the free surface a distance $3.2h$ from the wavemaker as computed by OXPOT (black) and predicted by linear theory (red) for sea state SS1.

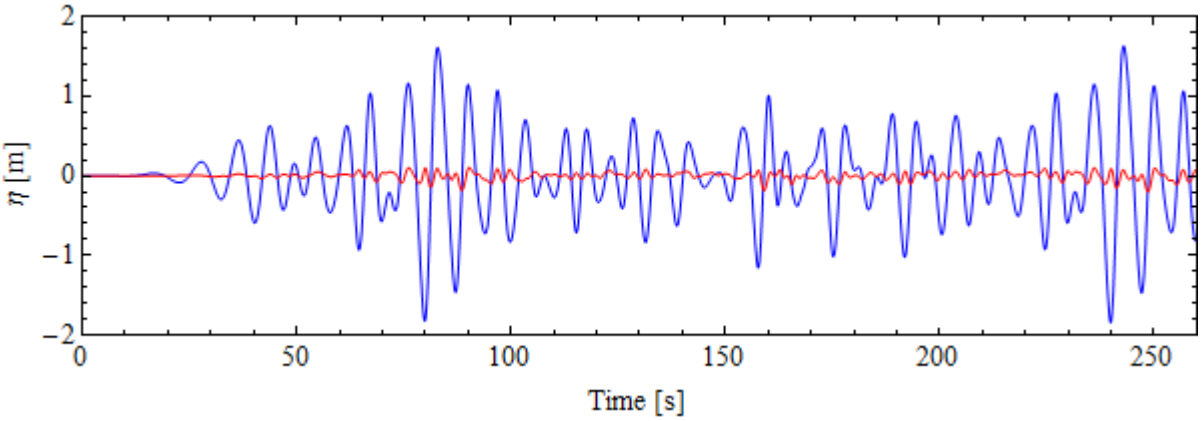

Figure 4: Odd harmonics (blue) and even harmonics (red) of the incident wave.

For sea state 2, where the energy period is $T_e = 8.0s$ and the peak period is approximately $T_p = 9.3s$ the corresponding wavelengths are $\lambda_e = 1.99h$ and $\lambda_p = 2.64h$, respectively. In this case, the domain is specified to have a length of $L_D = 12.0$ with the wavemaker positioned at $x = -6.0$ so that a cylinder centred on $x = 0$ will be more than two peak wavelengths from the wavemaker. At the other end of the domain the damping zone was specified to be 1.5 peak wavelengths in length. The triangular free-surface elements are chosen to have a side of $\Delta x = 0.125$ so that there

are 21 elements per peak-wavelength, 16 per energy wavelength and 10 elements per second-order sum bound wavelengths. Given that each element has 6 nodes, this was considered sufficient to describe second order wave propagation. Nevertheless, contributions from wave components more than twice the peak frequency may not be fully resolved. In terms of time-advancement algorithm, the time-step was specified to be $\Delta t = T_e/40$ and so a simulation of a repeat period $T_r = 25\,T_e = 200s$ involves 1000 time steps. As before, to allow time for the incident wave to arrive at the origin it is necessary to simulate a repeat period and a half and so the number of time-steps is approximately 1500 in this case.

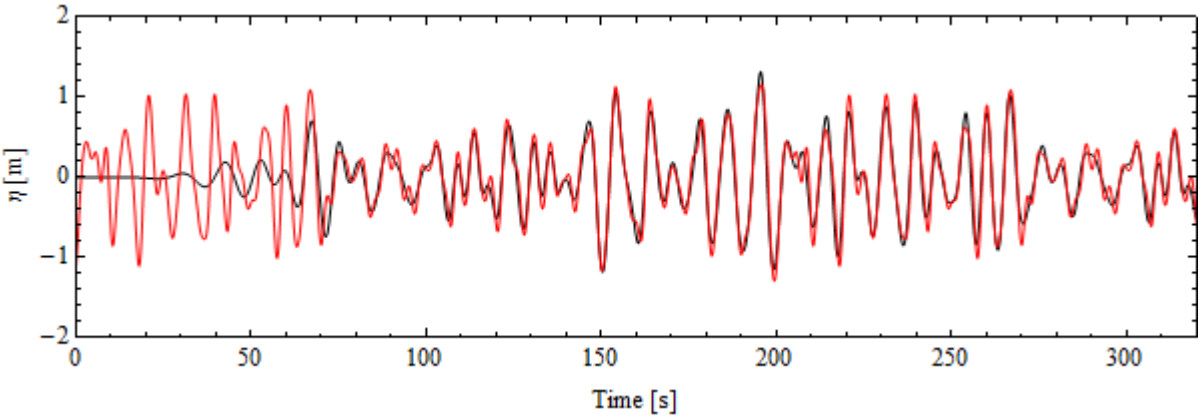

Figure 5: Free surface elevation at a point on the free surface a distance $6.0h$ from the wavemaker as computed by OXPOT (black) and predicted by linear theory (red) for sea state SS2.

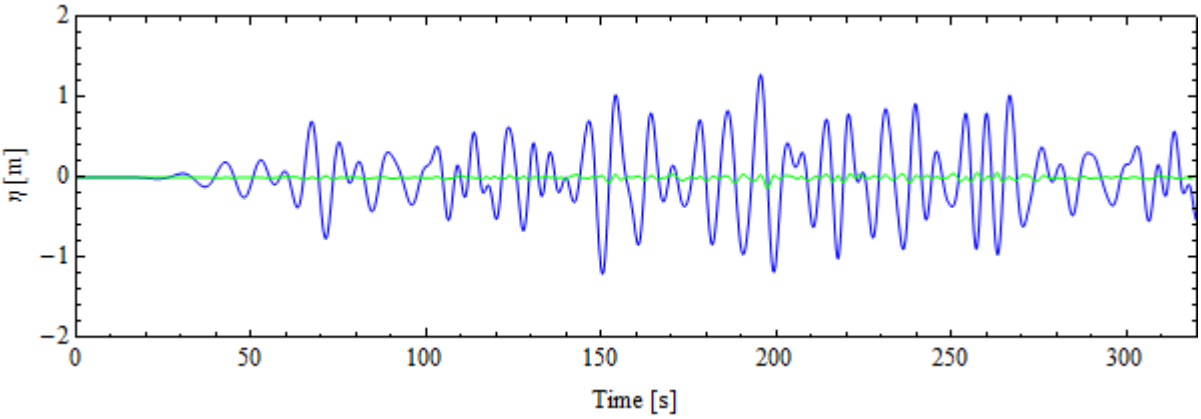

Figure 6: Odd harmonics (blue) and even harmonics (green) of the free-surface elevation signal.

The comparison of the free-surface elevation computed at the origin by OXPOT and to the linear prediction is shown in Figure 5 where a reasonably good agreement is obtained. It is clear that some of the high frequency wave forms are not resolved properly and this is most likely due to the relatively coarse meshing which was used. Such a mesh is necessary in order to simulate a large area of free surface, such as in the case where the body is present, without associated long simulation durations. The comparison of the first and second order components of the total free-surface elevations in Figure 6 illustrates how weak the nonlinearity is in this sea state. To afford the opportunity of observing nonlinearity in the device interaction simulations it is necessary to increase the significant wave height considerably. Therefore, the next simulations involve waves with

identical phases to those used for the results presented in Figure 5 and Figure 6 but with the wave amplitudes three times larger – this sea state is denoted SS6. It is clear from comparing Figure 8 to Figure 6 that the second order contribution is now non-negligible. It should also be noted that the comparison of linear (theory) and fully nonlinear (computational) free-surface elevations reveals significant discrepancies. These discrepancies are not only due to higher order contributions – it is likely that the large motion of the end wall (wavemaker) which introduces horizontal free-surface node motion also affects the computed values because the free-surface elevations are computed at the nodes closest to the specified location and not at the location itself. This effect will be more significant for larger waves which require larger wavemaker excursions and, thus, larger nodal motions. To extract the free-surface elevation at a fixed point it is necessary to output the free-

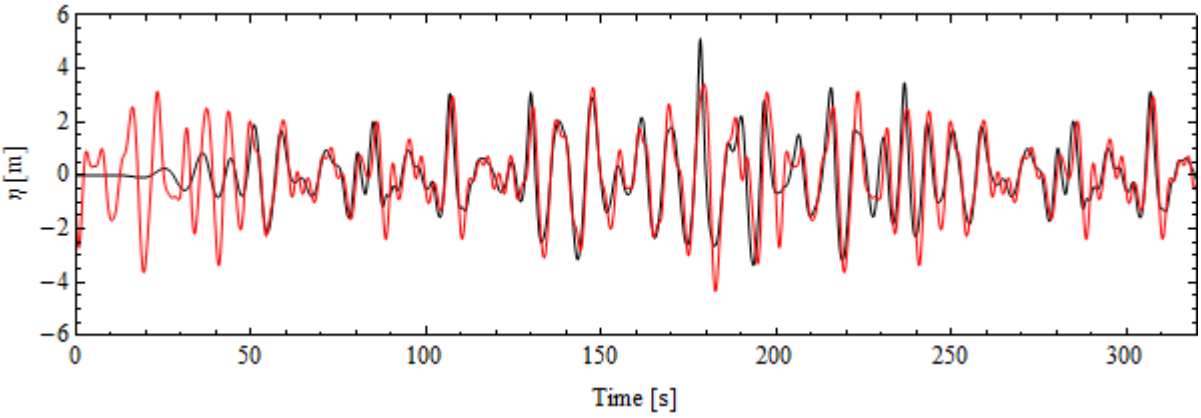

Figure 7: Free surface elevation at a point on the free surface a distance $4.0h$ from the wavemaker as computed by OXPOT (black) and predicted by linear theory (red) for sea state SS6.

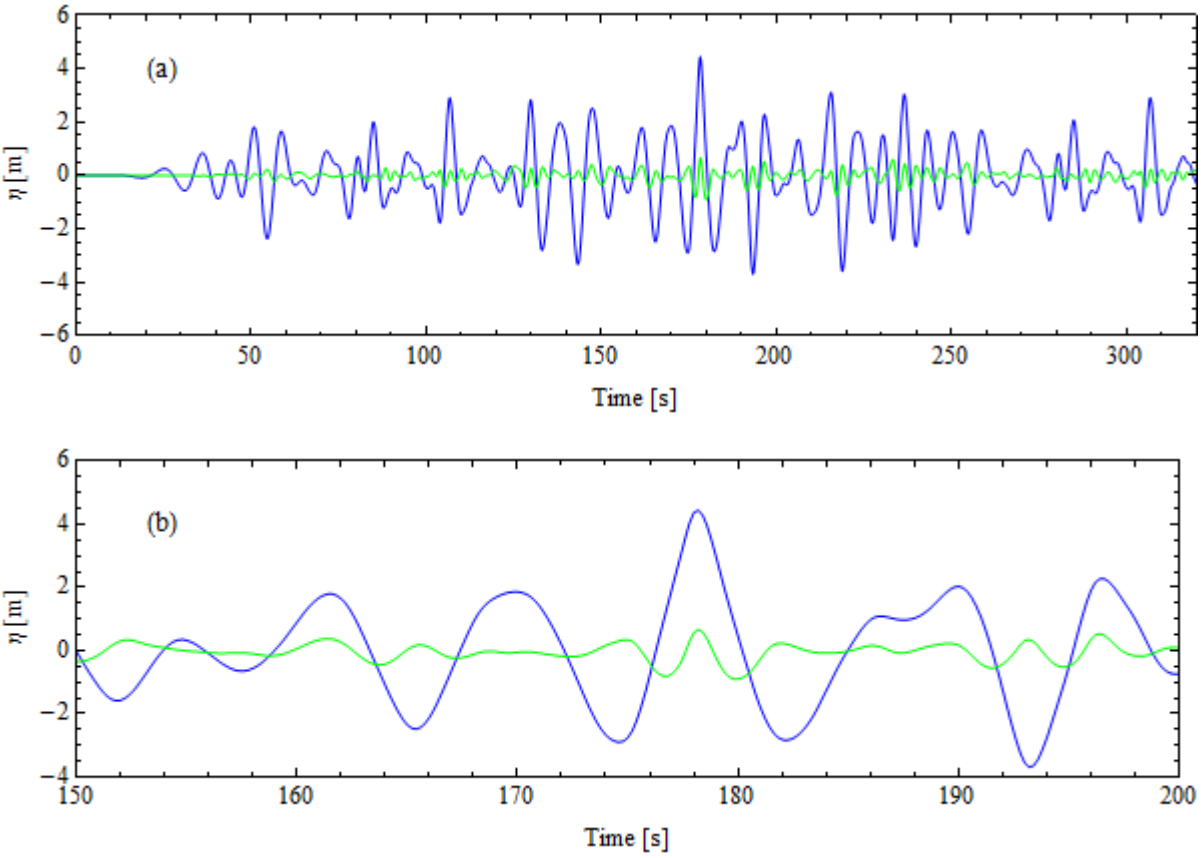

Figure 8: Odd harmonics (blue) and even harmonics (green) of the free-surface elevation time-history at a distance $4.0h$ from the wavemaker for SS6 for (a) the whole simulation and (b) a short time interval around a large wave crest.

surface elevation at a number of adjacent nodes around the fixed point and to interpolate the free-surface elevation value at the fixed point.

It is useful to note some of the structure of the second order bound waves. For the large crest at $t \simeq 179s$ the second order wave can be seen to contribute quite considerably to the total wave amplitude. Furthermore, the wave follows the classic Stokes' type structure for a large crested wave whereby the peak is further enhanced by the presence of the bound wave but the troughs either side of the peak are mitigated by the form of the second order wave. Given that a first order wavemaker signal is used to generate the waves there will also be wavemaker-produced error waves (also referred to as spurious waves) propagating down the tank; however, these error waves are not bound to the first order wave and it can be expected that the bound second order waves will dominate in particular for large wave events such as that highlighted in Figure 8 (b).

3 IRREGULAR WAVE SIMULATIONS FOR SINGLE DEVICES

3.1 Mesh for the rounded end cylinder

In previous deliverables the excitation forces, responses and power absorption values were investigated for regular waves incident on truncated vertical cylinders. However, in experimental work conducted by QUB reported in WG2 WP2 D5 the wave energy devices were modelled as rounded vertical cylinders whereby a truncated cylinder was rounded by the addition of a hemispherical end. Thus, it was decided, with future experimental validation work in mind, to investigate the performance and operation of rounded cylinders in irregular waves.

In OXPOT, the mesh for the truncated cylinder is straightforward to generate. A small adaptation of the truncated meshing routine allows the rounded end to be meshed also. Although easy to implement, this adapted mesh procedure is not the best approach for discretising a hemispherical surface and some minor issues arise because of its application. For truncated cylinder geometries,

the planar truncated surface is discretised using the Delaunay triangulation method as described in (Bai & Eatock Taylor, 2006) and is summarised in the following. Firstly, a set of points on the circumference of the bounding circle which encloses the truncated cylinder surface are generated from the discretisation of the vertical cylinder surface. These points are the set of corner nodes (i.e. not mid-point nodes) of the quadrilateral elements which discretise the vertical cylinder surface. This set of bounding points forms an initial basis set of coarse triangles which are made finer by the insertion of more points within the planar domain. The number of extra points added is an OXPOT input and this controls the fineness of the triangulation. However, at the boundary of the truncated surface the triangle size depends on the fineness of the circumference discretisation. Mid-point nodes are then generated based on the vertices of the Delaunay triangles. Such mid-point nodes are necessary in the higher order boundary element method to represent the position coordinates, velocity potential and its derivative within an element in terms of the nodal values using quadratic shape functions as described in section 2,3 of WG1 WP1 D7. Each mid-point node that lies between two vertices of a triangular element which discretise the cylinder circumference are prescribed to lie on the circumference also – as standard the mid-point nodes are positioned on the line joining the two vertices. For the rounded cylinder with the hemispherical bottom, this 2D triangulation is applied once more to determine the (x, y) coordinates of the nodes. The z-coordinates are determined from the equation for the surface of the hemisphere $z = -d - \sqrt{a^2 - (x^2 + y^2)}$ where d is the draft of the cylinder in equilibrium and a is the radius of the cylinder and also the hemisphere. An example of the resultant mesh for a cylinder in a simulation where no symmetry is assumed is shown in Figure 9. It is clear from this illustration that although the 2D mesh is effective at discretising the surface at locations where the rate of change of the vertical coordinate is relatively small it is not effective at the sides of the hemisphere. In particular, the triangular elements at the vertical surface boundary are quite distorted from the ideal equilateral triangle case. Another discretisation method involving a more structured grid was also attempted but when the results of regular wave simulations were compared, no significant improvements were observed. Therefore, it was decided that the modified 2D triangulation method would suffice. In Figure 9, the triangles are generated in the plotting program by joining the vertex nodes of a given six node element. In OXPOT the mid-point nodes are not constrained to lie on the plane of the triangular planes formed by the three vertex points. Instead the nodes are prescribed to satisfy the equation for the surface of the hemisphere. Hence, the nodes in the side-view plot in Figure 9 do not align with the triangles representing the elements.

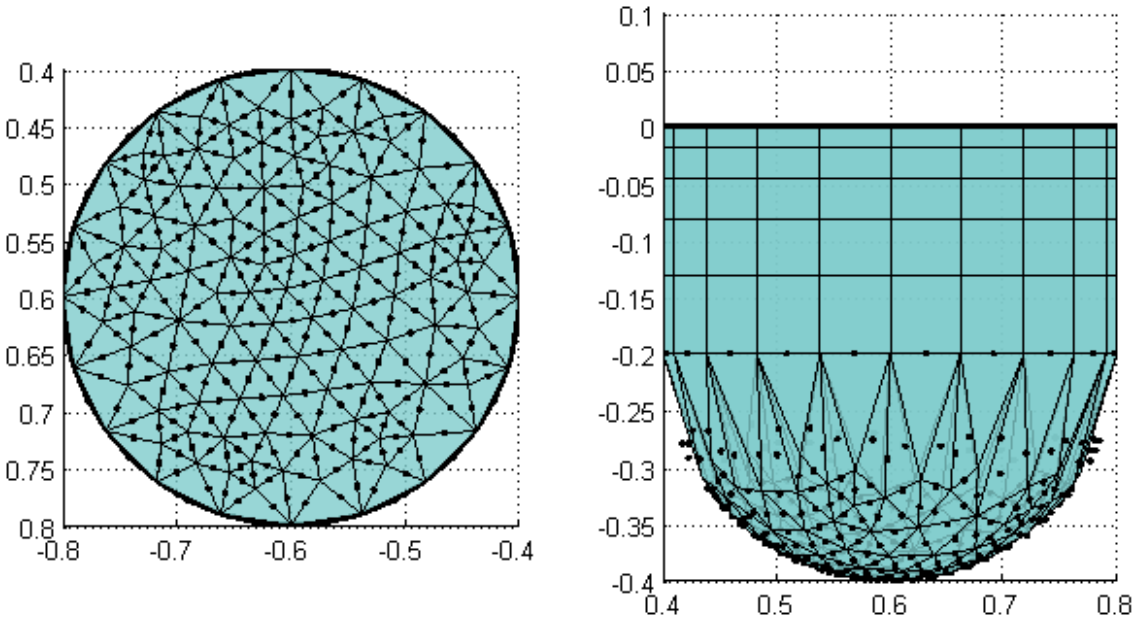

Figure 9: Rounded vertical cylinder as view from below (left) and from the side (right). On the rounded surface the mid-point nodes of the triangular elements are included.

In simulations where the discretisation is relatively coarse the reduction in discretised volume of the cylinder with the rounded end means it is not initially in equilibrium and so 'sinks' very slightly in an oscillatory fashion to its actual equilibrium. However, as the number of circumference elements on the vertical boundary increases the length of the sides of the triangles at the boundary of the vertical and hemispherical surfaces will decrease with a consequent reduction in the discretisation error. The number of elements on the circumference of the cylinder must be chosen so that the triangular elements on the intersecting free-surface are not distorted either – these triangular elements are chosen based on peak incident wavelength and so for longer incident waves the cylinder mesh is generally coarser and the discretisation error larger. The geometry specifications of the cylinder with the rounded end, which is used in all the subsequent simulations, in terms of the water depth h are as follows: the vertical truncated section has a radius of $0.2h$ and a draft of $0.2h$ and the hemisphere has a radius of $0.2h$ giving a total draft $0.4h$. In the subsequent discussions in this report the term 'device' is used to interchangeably with the term 'rounded vertical truncated cylinder'.

3.2 Modelling long lines of devices

In OXPOT simulations involving axisymmetric devices in unidirectional seas it is natural to align the coordinate axes so that the device surge motion occurs along the x-axis and that the direction of the sway mode (although not excited) is along the y-axis. It follows from the assumption that no sway motion is excited that the fluid motion throughout the domain will be symmetric about the y-axis so that $\partial\phi/\partial y = 0$, where ϕ is the velocity potential. In this case, it is necessary only to solve the water-wave problem on the half-domain with non-negative y coordinates. At the surface of symmetry $y = 0$ the boundary condition $\partial\phi/\partial n = 0$ is obeyed and so the surface of symmetry is treated as a wall with a no-flow condition. If the BEM is used to solve the water-wave problem then in the boundary integral equation formulation preceding the BEM some terms corresponding to integration along this wall of symmetry will arise. These can be eliminated by choosing the Green's

function to satisfy $\partial G/\partial y = 0$. The Green's function is the Rankine source and its image with respect to the plane of symmetry $y = 0$ as described in section 2.3 of WG1 WP1 D7.

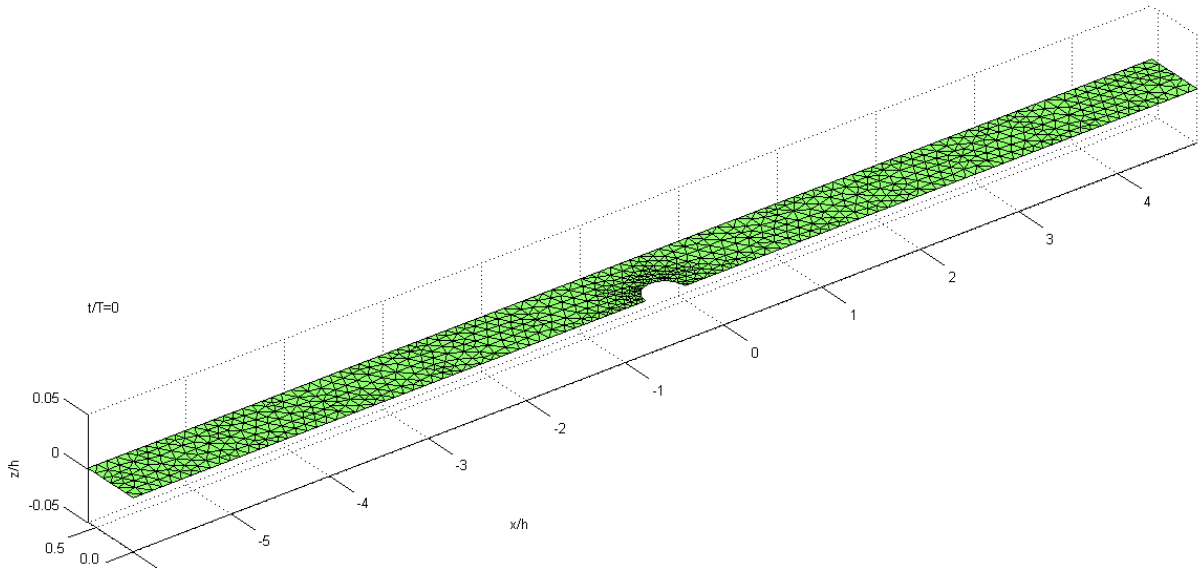

Figure 10: Half-domain modelling an infinitely long line of devices perpendicular to the direction of wave incidence (along the x-axis).

To apply the boundary integral equation it is necessary to have outer boundaries enclosing the fluid domain. In OXPOT, these outer boundaries are vertical and either perpendicular (the wave-maker and end wall) or parallel (the side wall) to the direction of wave propagation. On the side wall a no-flow boundary condition is applied $\partial\phi/\partial y = 0$; however, it is not possible to eliminate integration on this wall because the Green's function cannot be modified in a simple manner to satisfy $\partial G/\partial y = 0$ on $y = 0$ and $y = W$ where W is the half-width of the domain. Instead, the no-flow boundary condition $\partial\phi/\partial y = \partial\phi/\partial n = 0$ must be satisfied on the side wall in the BEM. In the OXPOT simulations described in D9 and D10 it has been mentioned how this wall boundary condition leads to reflections and thus why it is necessary to have wide domains where possible to minimise the effect of these reflections. However, although the boundaries are treated differently in the BEM the physical boundary conditions are identical on each surface. Thus, just as the boundary condition $\partial\phi/\partial y = 0$ at $y = 0$ implies symmetry, so the same condition at $y = W$ corresponds to a wall of symmetry. Therefore, a single half domain with a free-surface such as that shown in Figure 10 corresponds to an infinite line of structures perpendicular to the direction of wave incidence. In this manner, we will model the operation of a long line of closely spaced devices. As the width of the domain increases, the reflected scattered and radiated waves become smaller due to the $1/\sqrt{r}$ decay of the wave amplitudes, and so the device operation approximates that of a device in isolation. However, the reflecting boundary condition is identical in both the 'isolated' device simulations and the simulations of long lines of units.

Two lines of devices were considered, one with an inter-device spacing of three diameters and one of five diameters. Of interest is both the effect of the device spacing on the power absorption capabilities of the devices and also the device response. A linear PTO only is considered – more general PTOs will be considered in the case of a single device operating in isolation – and the PTO damping coefficient is $3.043 \times 10^5 Nm^{-1}s$. To further restrict the number of simulations that must

be run, the power absorption in sea state 2 only is considered. The responses and instantaneous power absorbed for devices in an infinite line with a spacing of three diameters and five diameters are compared to that of a device in a domain of width $3.25h$ (approximating a device in isolation) in Figure 11.

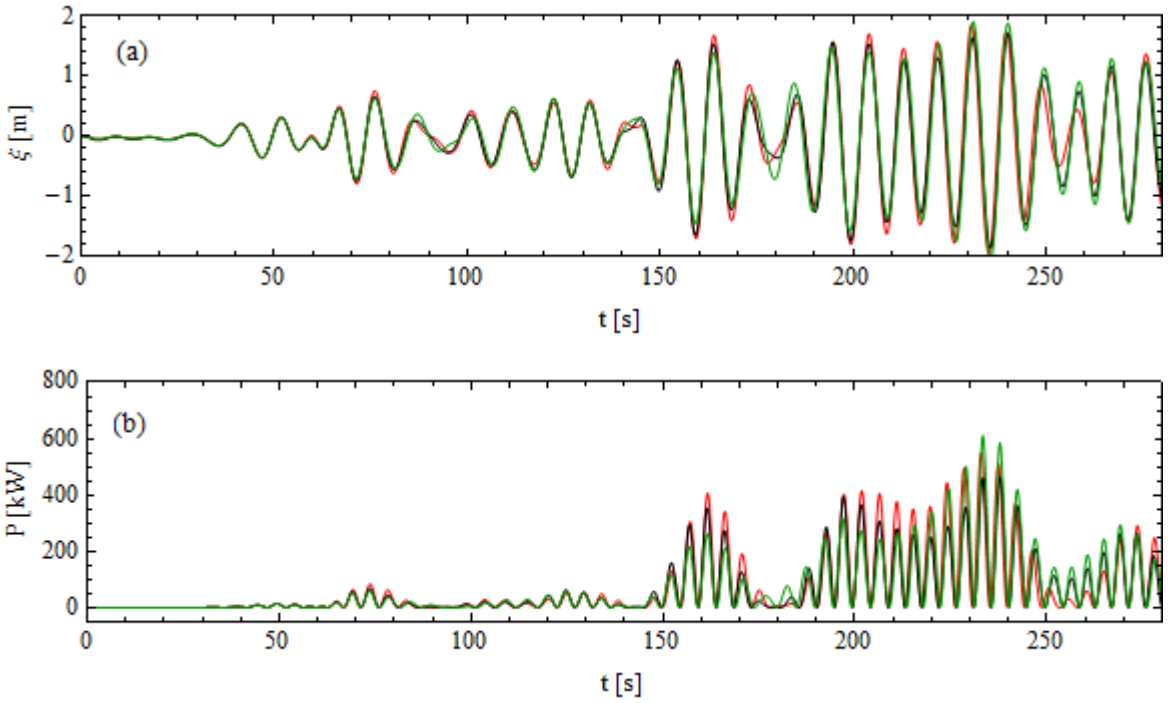

Figure 11: Response and power take-off for a single device in an infinite row of devices spaced three diameters (red), five diameters (green) and in effective isolation (black).

There are clear interaction effects due to the presence of the neighbouring bodies which are visible as differences in the response time-histories around $180s$ and $250s$ in particular. In other intervals during the time history the response is more uniform because the incident wave excitation dominates the reflected and diffracted waves. Once the device has moved with relatively large motions (where the amplitude is greater than $1m$) then the effects of the radiated waves, which take different times to arrive at the neighbouring bodies depending on the inter-device distance, can be observed when the amplitude of motion excited by the incident wave becomes smaller, e.g. at $t \simeq 180s$ and $t \simeq 250s$. The effect of the inter-device spacing on the radiated waves is best illustrated by plotting the simulated free-surface surrounding the single device and using symmetry to replicate the free-surface around a number of the devices in the long line. A comparison of the free-surface snapshots at the same simulation time, shown in Figure 12 and Figure 13, for a device spacing of three diameters and five diameters, respectively, illustrates how the radiated waves will take longer to arrive at the neighbouring devices in the case of the larger device spacing. Furthermore, the radiated waves will be relatively weaker when arriving at the neighbouring device when the spacing is five diameters compared to a spacing of three diameters.

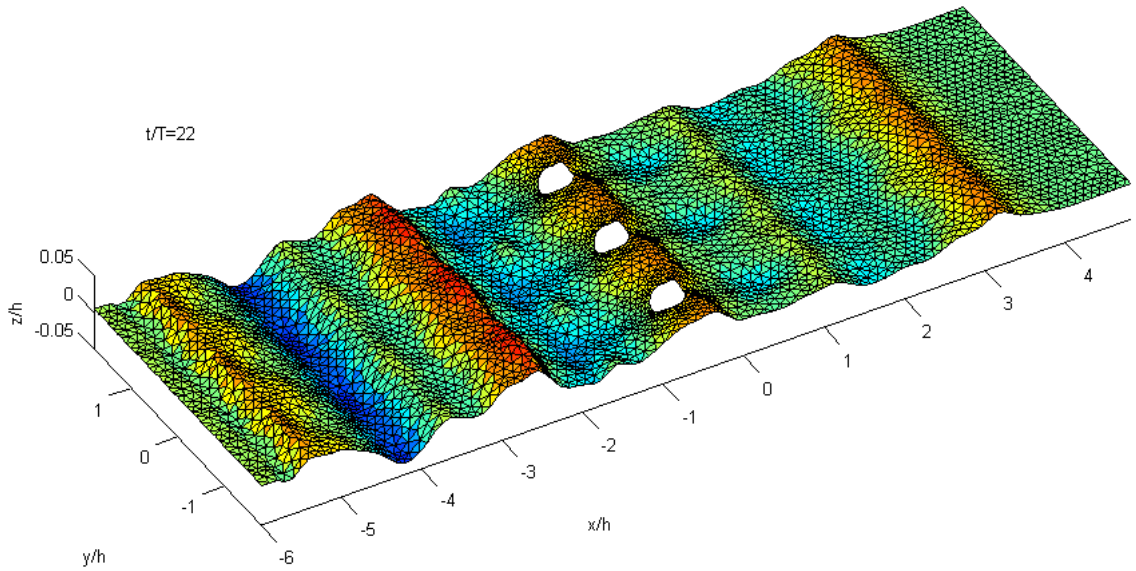

Figure 12: A plot of the (symmetric) free-surface elevation for three devices in an infinite line of devices with an inter-device spacing of three diameters.

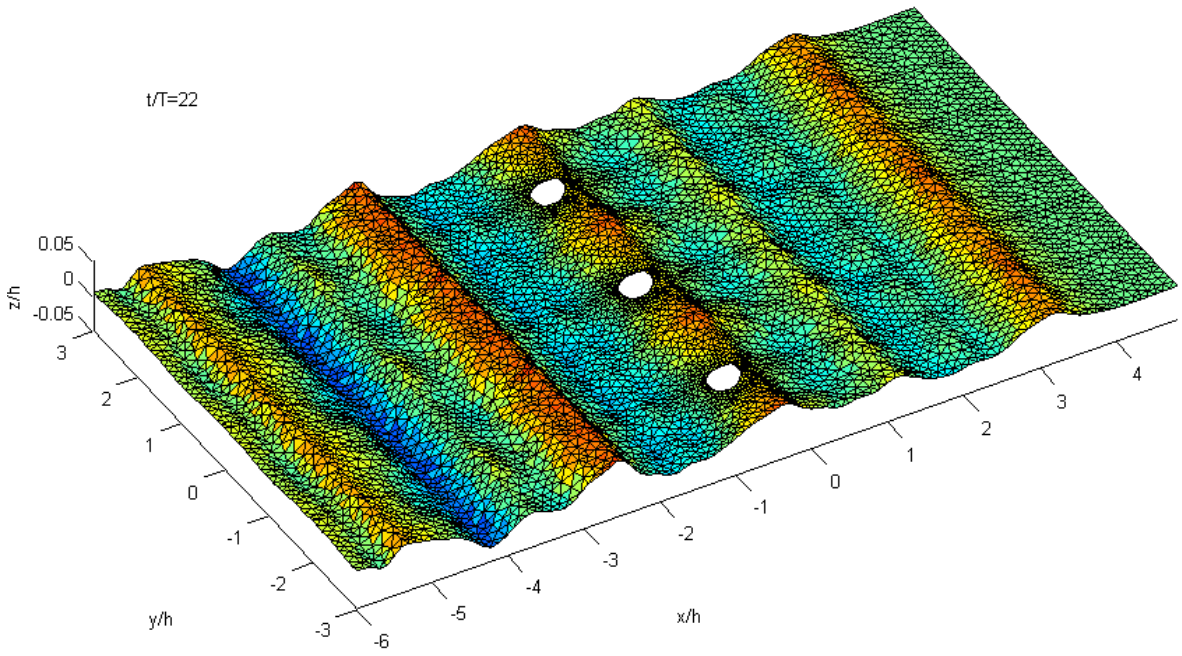

Figure 13: A plot of the free-surface elevation for three devices in an infinitely long line of devices with an inter-device spacing of five diameters.

The instantaneous power absorbed by the power take-off mechanism is given by

$$P_{ABS}(t) = F_{PTO}(t)\dot{x}(t), \tag{9}$$

where $\dot{x}(t)$ is the heave velocity of the device and $F_{PTO}(t) = c_{PTO}\dot{x}(t)$ for a linear PTO so that

$$P_{ABS}(t) = c_{PTO}\dot{x}(t)^2 \tag{10}$$

for a linear PTO. The average power absorption is computed using

$$P_M = \frac{1}{T_2 - T_1}\int_{T_1}^{T_2} P_{ABS}(t)dt \tag{11}$$

and so it is necessary to choose the absorption interval (T_1, T_2) over which to compute the average. In these simulations involving irregular waves from sea state 2, the incident waves were generated in an identical manner to that described in section 2.2. Therefore, the incident waves had a return/repeat period of $200s$ and the power absorbed is averaged over the final $200s$ of the simulation on the interval $(T_1, T_2) = (80s,\ 280s)$. During this interval, the mean power-absorbed by the devices with a spacing of 3 diameters is $92.0kW$ and for 5 diameters it is $89.2kW$. In contrast, for the device operating in approximate isolation (with a domain of width $3.25h$) the mean power absorbed is $83.4kW$. Therefore, for the current realisation of this particular sea state and for this particular device it is beneficial on average to have the devices operating in a line spaced either 3 or 5 diameters apart. The mean power capture results are summarised in Table 3 and include the results for the device operating in effective isolation for comparison.

Spacing	Wavelength λ_p/h	Wave height H_s/h	Length L/h	Half-width W/h	Number of Elements	Number of Nodes
3 diameter	2.64	0.04	10.8	0.6	3061	8539
5 diameter	2.64	0.04	10.8	1.0	4021	10899
Wide	2.64	0.04	10.8	3.25	5822	15164

Table 2: Computational domain details for the single body simulations involving incident sea state 2.

Device spacing	PTO specification		Mean power capture (P_M)
	$k_{PTO}/(Nm^{-1})$	$c_{PTO}/(Nm^{-1}s)$	
3 diameters	0.00	3.043×10^5	$92.0kW$
5 diameters	0.00	3.043×10^5	$89.2kW$
Effective isolation	0.00	3.043×10^5	$83.4kW$

Table 3: Summary of mean power capture results for long lines of units.

3.3 Simulation results for a device in isolation in sea state 2

3.3.1 Effects of different PTO damping forces on power capture

The performance of a single isolated body (i.e. corresponding to the widest domain in Table 2) with a number of different PTO configurations have been simulated for a single isolated body in irregular waves from sea state 2. The irregular waves are generated in an identical fashion to that described in

section 2.2.1; however, the simulations are more complex because the computational domain is wider and contains the rounded circular cylinder. A visualisation of the free-surface during one of these simulations is shown in Figure 14. Note that only half of the domain is simulated using symmetry arguments described in the last section but the total free-surface is shown for the purposes of visualisation. The unstructured triangular elements on the free-surface are plotted as flat panels in this visualisation; however, the variation of the boundary data on the elements themselves is quadratic and each element is discretised by three vertex nodes and three mid-point nodes. The computational details of the domain are summarised in entry labelled 'Wide' in Table 2. Further to the information in this table, it should also be mentioned that the total domain is divided into five sub-domains. All simulations for sea state 2 utilised this computational domain with the input parameters pertaining to the body and PTO force altered in order to investigate the effects of PTO and control variations on the average power absorbed.

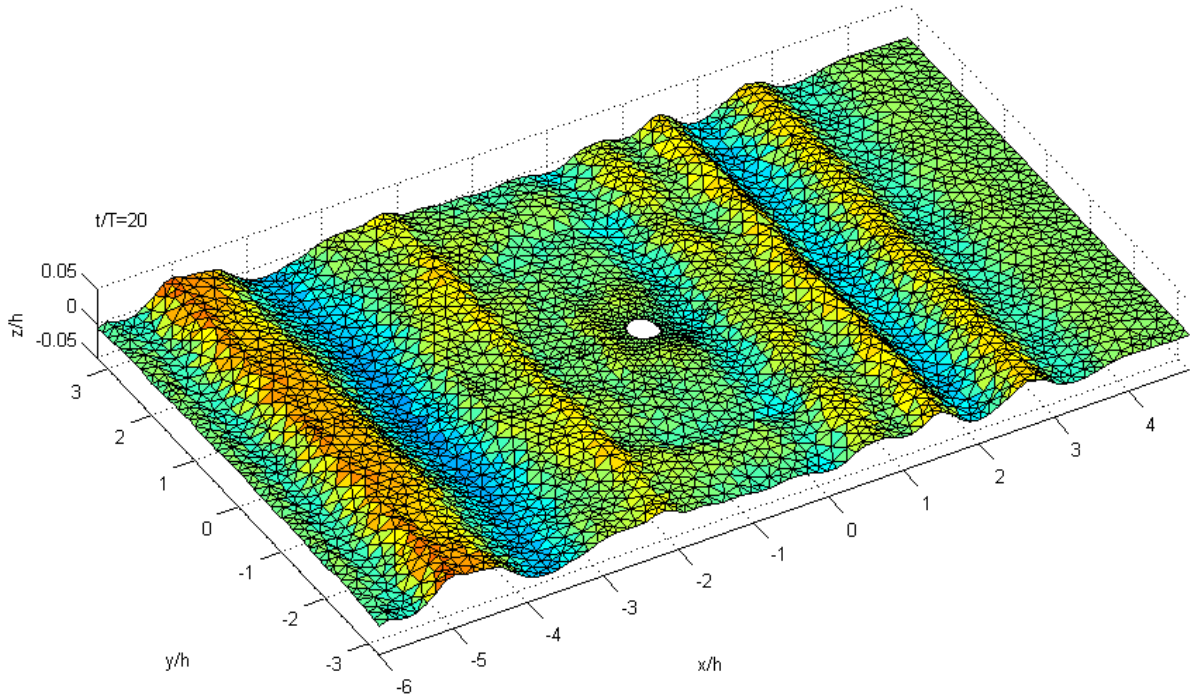

Figure 14: Visualisation of the free-surface during a simulation of irregular wave incidence on a rounded cylinder.

For sea state 2, a simulation of power absorption with the PTO damping coefficient equal to the optimal value for a regular wave of period equal to the peak period (approximately $9.3s$) of the spectrum is conducted. With no PTO restoring force the optimal damping coefficient for a monochromatic (regular) wave of angular frequency ω is

$$c_{PTO} = \left\{ b(\omega)^2 + \left(\omega(m + a(\omega)) - \frac{(\rho g\, W)}{\omega} \right)^2 \right\}^{1/2} \tag{12}$$

where a and b are the added mass and damping coefficients for the rounded vertical cylinder at ω, m is the mass of the cylinder, ρ the density of water and W is the water-plane area. For the peak frequency of the sea state 2 spectrum the optimal PTO damping coefficient for a zero restoring force is determined to be $3.043 \times 10^5 Nm^{-1}s$. As part of WG1 WP2 D4, comparisons between the power

absorption results from the spectral wave model and the fully nonlinear model are made for the case of a square array of four devices. The PTO coefficient used by QUB for WG1 WP2 D4 is $c_{PTO} = 7.0 \times 10^6 Nm^{-1}s$ which is an order of magnitude larger than the optimal peak frequency value. If the system is characterised as a damped harmonic oscillator then this PTO damping is close to the critical damping value.

In the following discussions, the PTO damping coefficient optimised for the peak frequency is referred to as the 'weak' damping case and the latter as the 'strong' damping case. Therefore, the response and power absorption time-histories for the device subject to both of these linear PTO dampers were computed and compared in Figure 15. It is clear that the strongly damped case reduces the response of the device considerably (possibly a factor of 10) compared to the weakly damped case. In terms of the power absorbed, the power absorbed by the device subject to a small PTO damping is significantly larger than for the large PTO damping with time-averages over the last 200s computed as $83.4kW$ and $31.5kW$, respectively. These values are relatively close because, despite the large difference in the motion amplitudes as seen in Figure 15 (a), the weakly damped device significantly outperforms the strongly damped device only in the final 80s of the simulation as is evident in Figure 15 (b). It is worth noting that the incident irregular waves have a peak period $T_p \simeq 9.3s$ and the device has a natural resonant period of approximately $9.0s$. Thus, the device will frequently heave at or near resonance and such resonant motions will yield significant power capture. For the weakly damped device such resonant motions result in displacement amplitudes of one metre or more whereas the strongly damped device only moves about $20cm$ with a consequent reduction in velocity amplitudes also. Therefore a large reduction in displacement amplitude due to strong damping will not benefit the power absorption capability of the device.

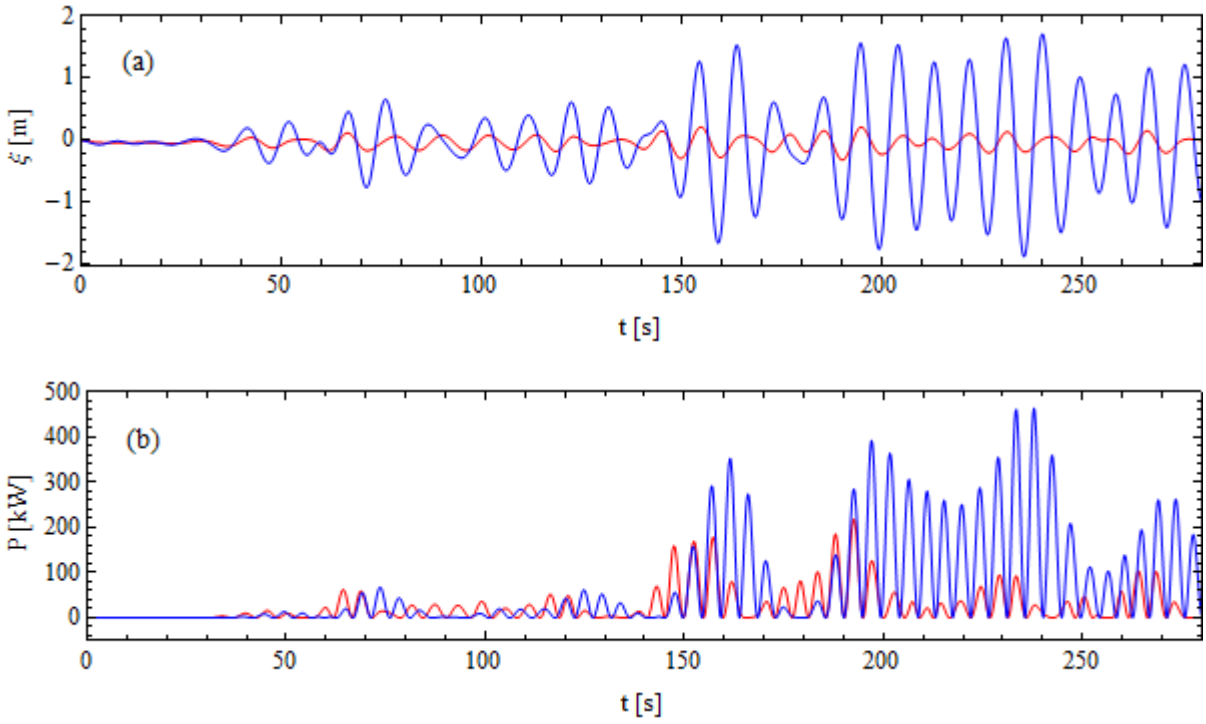

Figure 15: Comparison of (a) the heave response of a single device in incident sea state 2 and (b) the instantaneous power absorption for weak (blue) and strong (red) linear PTO damping.

To model the wave energy converter brake used to extract energy from the converter motion in the experimental tests conducted by QUB for WG2 WP1 D5 it is necessary to implement a Coulomb damping PTO force in OXPOT. This is a sliding friction force which is independent of displacement and always opposes the motion. This is modelled as

$$F_{PTO-C}(t) = \begin{cases} -D, & for\ \dot{x}(t) > 0 \\ D, & for\ \dot{x}(t) < 0 \end{cases}. \tag{13}$$

where μ is the magnitude of the friction force. A large Coulomb damping PTO force in an irregular sea may result in significant intervals of 'stall' whereby the device remains fixed in position because the hydrodynamic forces on the device are not sufficient to overcome the PTO force. Although we do not model the transition from static to kinetic friction that will occur with an actual friction brake when stall occurs it is expected that the OXPOT simulation will represent intervals of stall (where the wave force is not significantly larger than the Coulomb friction force) as small unsteady body motions. To demonstrate that OXPOT can simulate the wave-device interactions involving this nonlinear PTO force power absorption through a Coulomb friction PTO mechanism with a large magnitude for the opposing force is simulated. The target Coulomb damping force in the QUB experimental tests ($0.4N$ at 1:80 scale) was not used as it is quite a weak damping force and hence the response of the device was not expected to differ much from a weak linear damping force.

To model a relatively large Coulomb damping force in a particular irregular sea it is useful to use the results of the simulation of a large linear damping force c_{PTO} in that same irregular sea as a reference point. The magnitude D of the Coulomb damping force is chosen to be comparable to the linear damping force c_{PTO} by the relation

$$D = c_{PTO}\hat{v} \tag{14}$$

where $\hat{v}$ is the r.m.s. velocity computed over a full repeat period. Using the results of the linear damping simulation with $c_{PTO} = 7.0 \times 10^6 Nm^{-1}s$ as reference the magnitude of a comparable Coulomb damping force is determined to be $D = 4.69 \times 10^5 N$. The response and instantaneous power capture as computed by OXPOT for a device moving subject to this Coulomb damping force are compared to the strong linear damping case in Figure 16. The occurrence of 'stall' for the device subject to the Coulomb friction force is evident during the time interval $(70s, 140s)$ where only very small motions occur (although only faintly visible for the scale used in Figure 16). Further evidence of the wave force not overcoming the Coulomb friction force is visible at time $t \simeq 250s$. Nevertheless, the magnitude of the Coulomb friction force does allow a relatively large response of the device when incident waves of larger amplitude excite the device motion. Therefore, the mean power absorption over the interval $(80s, 280s)$ of the nonlinear PTO $(71.8kW)$ is significantly larger than that of the strongly damped linear PTO $(31.5kW)$.

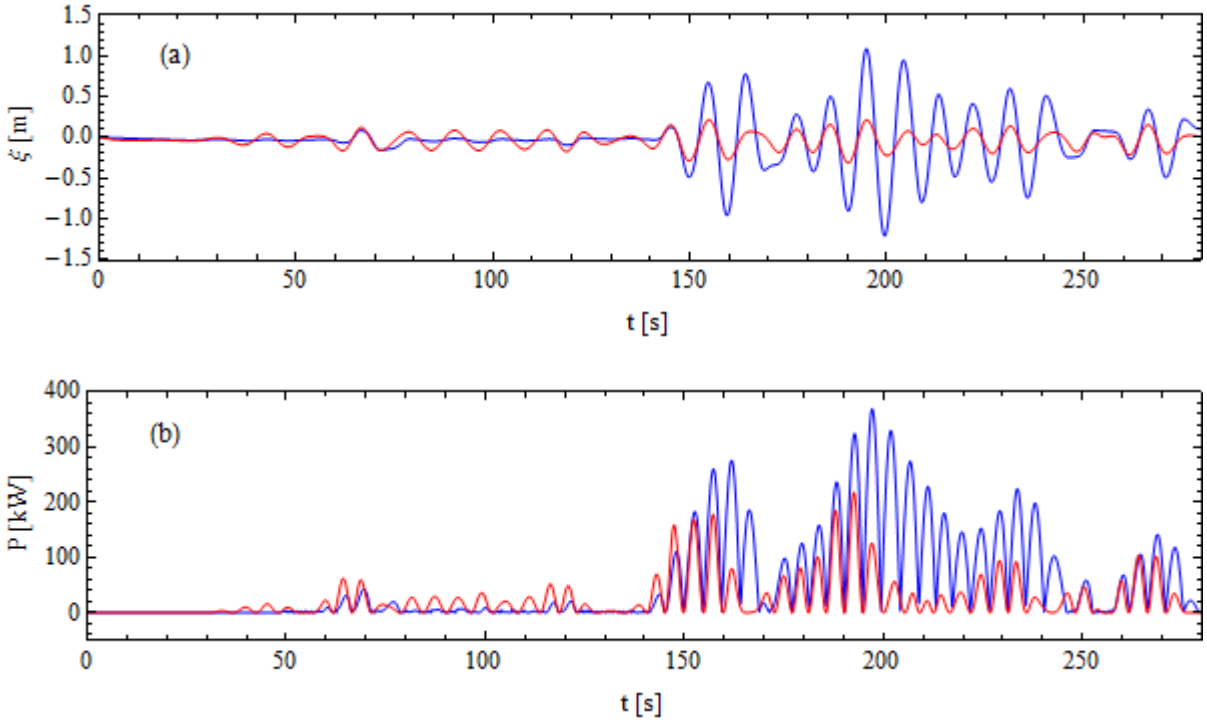

Figure 16: Comparison of (a) the heave response of the device and (b) the instantaneous power absorption of the device in SS2 subject to a linear (red) and Coulomb friction (blue) PTO force.

3.3.2 Effects of the PTO restoring force on power capture

For a linear PTO is also natural to include a restoring force component to the PTO force so that $F_{PTO} = k_{PTO}x(t) + c_{PTO}\,\dot{x}(t)$. To compute the mean power absorbed it is necessary to include only the damping term because the reactive power $k_{PTO}x(t)\dot{x}(t)$ has a net zero contribution provided the average is computed over a full repeat period. (For an averaging interval of sufficient length the mean reactive power will be close to zero even if the interval is not a full repeat period). However, as discussed in section 2.1 of WG1 WP1 D10 it is possible to optimise both the restoring force coefficient k_{PTO} and the damping coefficient c_{PTO} simultaneously to achieve optimal linear power absorption in regular waves. The optimal restoring force coefficient value which satisfies the resonance condition is

$$k_{PTO} = \rho g W - \omega^2(m + a(\omega)), \tag{15}$$

Where W is the waterplane area, and the corresponding optimal damping is

$$c_{PTO} = b(\omega). \tag{16}$$

For incident regular waves with frequency equal to the spectral peak ω_p, the optimal restoring force coefficient (or spring coefficient) is $k_{PTO} = -1.539 \times 10^5 Nm^{-1}$ and the optimal damping coefficient is $c_{PTO} = 2.034 \times 10^5 Nm^{-1}s$. The negative restoring coefficient is very difficult to implement practically and is potentially unrealistic and so we will not consider in detail device control involving negative spring coefficient values.

In models of PTO mechanisms, it is possible to have a small positive spring coefficient corresponding to a small restoring force acting on device through the PTO. We will consider a case where the spring coefficient is moderately large with an approximate value of $\rho gW/10$ corresponding to a change in the natural period of the device and PTO system to approximately $8.6s$. The natural frequency of the device and PTO is computed from

$$\omega_n = \sqrt{\frac{\rho gW + k_{PTO}}{m + a(\omega)}} \tag{17}$$

which involves rearranging the so-called resonance condition for wave energy converters (see WG1 WP1 D10 for more details). If the spring coefficient is non-zero then the optimal damping coefficient must be computed from

$$c_{PTO} = \left\{ b(\omega)^2 + \left(\omega(m + a(\omega)) - \frac{(\rho g\, W + k_{PTO})}{\omega} \right)^2 \right\}^{1/2}. \tag{18}$$

Evaluating this damping coefficient together with equation (15) at the peak frequency $\omega = 2\pi/T_p$ gives $k_{PTO} = 3.081 \times 10^5 Nm^{-1}$ and $c_{PTO} = 7.092 \times 10^5 Nsm^{-1}$, respectively. A comparison with the zero spring coefficient case and damping coefficient $c_{PTO} = 2.034 \times 10^5 Nsm^{-1}$ will be made. A further comparison to the power absorbed by a device subject to a linear PTO force with restoring/damping coefficients $(k_{PTO}, c_{PTO}) = (3.081 \times 10^5 Nm^{-1}, 2.034 \times 10^5 Nsm^{-1})$. In this way it will be possible to assess the relevance of the optimal linear PTO relations for regular waves to irregular waves and to understand how important a change in the resonant frequency of the device is when retaining the same damping coefficient.

Figure 17 shows the heave response and power absorption values for the three different linear PTOs. The inclusion of the spring restoring force changes the phase of the response of the device to the incident waves. This is particularly noticeable on the time interval $(200s, 250s)$ which is focussed on in Figure 18 where the peaks of the response of the device with a restoring PTO force applied and a damping coefficient $c_{PTO} = 2.034 \times 10^5 Nsm^{-1}$ consistently lead the peaks of the device with the same linear PTO damping but no restoring force. This is due to the change in the resonant frequency of the system mentioned previously. The average power absorbed over the last $200s$ of the simulation for the device subject to the restoring force is $70.2kW$ whereas in the absence of the restoring force it is $83.4kW$. Therefore, the power absorption capability of the device and PTO system is adversely affected by the inclusion of a PTO restoring force which changes the resonant frequency of the system to a value further from the peak incident wave frequency than the case of no PTO restoring force.

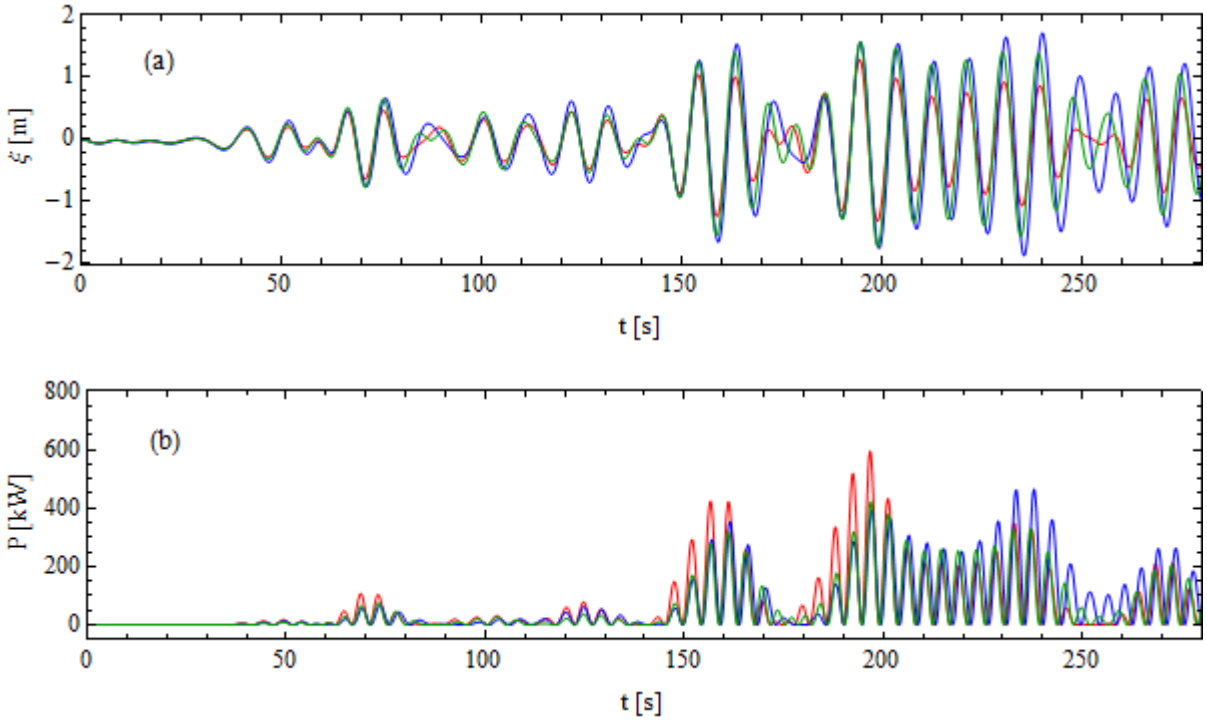

Figure 17: (a) Heave response and (b) power absorption time histories for device in sea state 2 with the following linear PTO coefficients: $(k_{PTO}, c_{PTO}) = (0.0Nm^{-1}, 2.034 \times 10^5 Nsm^{-1})$ blue line, $(k_{PTO}, c_{PTO}) = (3.081 \times 10^5 Nm^{-1}, 2.034 \times 10^5 Nsm^{-1})$ green line and $(k_{PTO}, c_{PTO}) = (3.081 \times 10^5 Nm^{-1}, 7.092 \times 10^5 Nsm^{-1})$ red line.

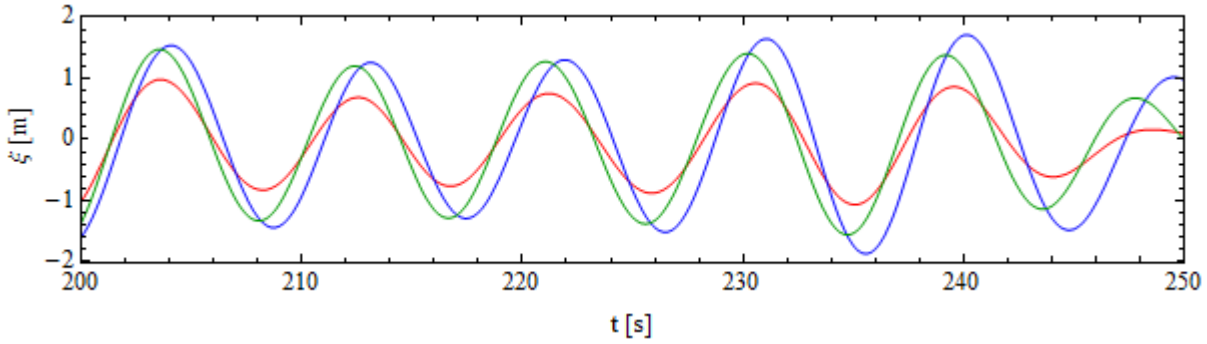

Figure 18: Heave response over the interval $(200s, 250s)$ for device in sea state 2 with the same linear PTO coefficients as in Figure 17.

However, if the linear PTO relation (18) is utilised to optimise the damping coefficient for the particular spring restoring coefficient used $(k_{PTO} = \rho g W/10)$ at the peak wave frequency $\omega = 2\pi/T_p$ it is possible to increase the average power absorbed. In this case, represented by the red line in Figure 17 and Figure 18, the damping coefficient is larger than the other cases and the response amplitudes smaller. The total power absorbed by this linear PTO is larger over some time intervals than the zero restoring force case (represented by the blue line); however, the average power absorbed over the last $200s$ of the simulation is $79.5kW$ compared to $83.4kW$ for the PTO without a restoring force term. Nevertheless, it is clear that the optimal linear PTO relations for regular waves are still useful for improving the power absorption properties of devices in irregular seas. Furthermore, matching the resonant frequency of the device to the peak frequency of incident sea state yields good power absorption (for this limited case-study, it yields the best value). A

summary of the mean power capture results for the isolated device in the same realisation of sea state 2 is presented in Table 4. The mean power absorption was computed over the interval $(80s, 280s)$ and the repeat period of the sea state realisation was $200s$. The terminology used in the preceding paragraphs was used to describe the simulations.

Simulation description	PTO specification		Mean power capture (P_M)
	k_{PTO}	c_{PTO}	
Weak damping	$0.0Nm^{-1}$	$3.043 \times 10^5 Nm^{-1}s$	$83.4kW$
Strong damping	$0.0Nm^{-1}$	$7.000 \times 10^6 Nm^{-1}s$	$31.5kW$
Coulomb	$0.0Nm^{-1}$	$4.690 \times 10^5 N$	$71.8kW$
Positive k_{pto}	$3.081 \times 10^5 Nm^{-1}$	$7.092 \times 10^5 Nm^{-1}s$	$70.2kW$
Optimised k_{pto}	$-1.539 \times 10^5 Nm^{-1}$	$2.034 \times 10^5 Nm^{-1}s$	$79.5kW$

Table 4: Summary of mean power capture results for an isolated device in the realisation of sea-state 2 described in section 2.2 for different PTO specifications.

3.4 Increasing the significant wave height of the incident sea state

To analyse the importance of nonlinearity in incident irregular waves on power absorption a more nonlinear sea state than SS2 is needed. Therefore, as described in the wave-generation section 2.2.1, a sea-state with identical phase components to sea state 2 but with the linear significant wave height increased from $H_s = 2m$ to $H_s = 6m$ is utilised in the analysis of power capture. An intermediate sea state with significant wave height of $H_s = 4m$ was also considered in order to assess how the increase in nonlinearity influences higher order contributions to average power capture. Therefore, simulations of the response and power capture of the device were conducted for the wavemaker signal which was two and three times larger than that used previously in this section and for the corresponding inverse signal. The second order contributions to forces and responses can be extracted as described in section 3.1 of deliverable WG1 WP1 D9. It should be noted that in a purely linear system the body motions and power absorption do not vary if the wavemaker signal is inverted. However, if there are second order contributions in the wave-field (not necessarily in the wavemaker signal) then this symmetry is lost and there should be a difference in both the body motions and, as a result, power capture in the seas generated by the original signal and its inverse. Therefore, the effect of second-order contributions should be visible in the power absorption time history of the more nonlinear sea-state. The second-order velocity contribution to the power absorbed first occurs in the power absorbed expression at third order in wave amplitude (as will be shown next) because the power absorbed has a quadratic dependence on velocity for a linear PTO.

It is assumed that the fully nonlinear free-surface elevation has a Stokes'-type structure dominated by the first and second order contributions. The elevation is expressed as a generalisation of the regular wave expansion

$$\eta(t) = a\cos\varphi + a^2(A_{20} + A_{22}\cos 2\varphi) + O(a^3), \tag{19}$$

where $a\cos\varphi$ represents the first order Fourier sum over wave components of amplitude a_n and phase φ_n and the a^2 term represents a double sum over wave components with A_{20} and A_{22}

representing the second order difference and sum coefficients. The irregular wave Stokes' expansion is represented in the form of a regular wave expansion because in this form it is more straightforward to demonstrate the ordered structure of hydrodynamic terms. If we assume this free-surface elevation is generated from a linear wavemaker signal $x_p(t;\varphi)$ with the set of component phases represented by φ then the inverted or phase-shifted wavemaker signal $x_p(t;\varphi+\pi) = -x_p(t;\varphi)$ will yield an elevation

$$\eta(t) = -a\cos\varphi + a^2(A_{20} + A_{22}\cos 2\varphi) - O(a^3). \tag{20}$$

For focussed wave groups it is typical refer to the waves generated from the (inverted) linear wavemaker signal $x_p(t;\varphi)$ $(-x_p(t;\varphi))$ as crest (trough) focussed waves and to use a subscript C (T) on all hydrodynamic quantities arising in the interaction. Therefore, the heave velocity for a device with a linear equation of motion in crest-focussed waves is given by

$$v_C(t) = a\,v_{11}\cos\varphi + a^2(v_{20} + v_{22}\cos 2\varphi) + O(a^3), \tag{21}$$

where v_{ij} represent wave-to-velocity transfer functions. The instantaneous power absorbed by a linear PTO is then given by

$$P^C_{ABS}(t) = c_{PTO}(a^2\,v_{11}^2\cos 2\varphi + a^3 v_{11}(v_{20}\cos\varphi + v_{22}\cos 3\varphi) + O(a^4)) \tag{22}$$

with a corresponding power absorption expression for the trough focussed wave

$$P^T_{ABS}(t) = c_{PTO}(a^2\,v_{11}^2\cos 2\varphi - a^3 v_{11}(v_{20}\cos\varphi + v_{22}\cos 3\varphi) + O(a^4)). \tag{23}$$

Therefore, by running two simulations with the inverted linear wavemaker signals and combining these power absorption expressions it is possible to obtain the power absorption due to first order velocity terms only and due to the combination of first and second order velocity terms.

The effect of the increase in nonlinearity in the incident irregular waves is more readily observable during a large wave event in the sea rather than considering the averaged power absorption which will also include intervals of approximately linear interactions. Therefore, the free-surface surrounding the device during a large wave interaction is considered. The complexity of the interaction may also depend on the size of body response. Such an interaction occurs around the device at $t \simeq 140s$ and the nonlinear nature of this interaction is evident from the free-surface elevation surrounding the cylinder (which corresponds directly to the run-up on the structure in a fully nonlinear simulation). The elevation of the free surface surrounding the structure is plotted for the three different sea state steepness values in Figure 19 and the wave elevations in the smaller sea states are linearly scaled to match those of the largest sea-state. Thus, if the interaction was completely linear then the free-surface would be identical in each case. However, it is evident from these free-surface plots that the wave at the structure is more pronounced for the largest sea state

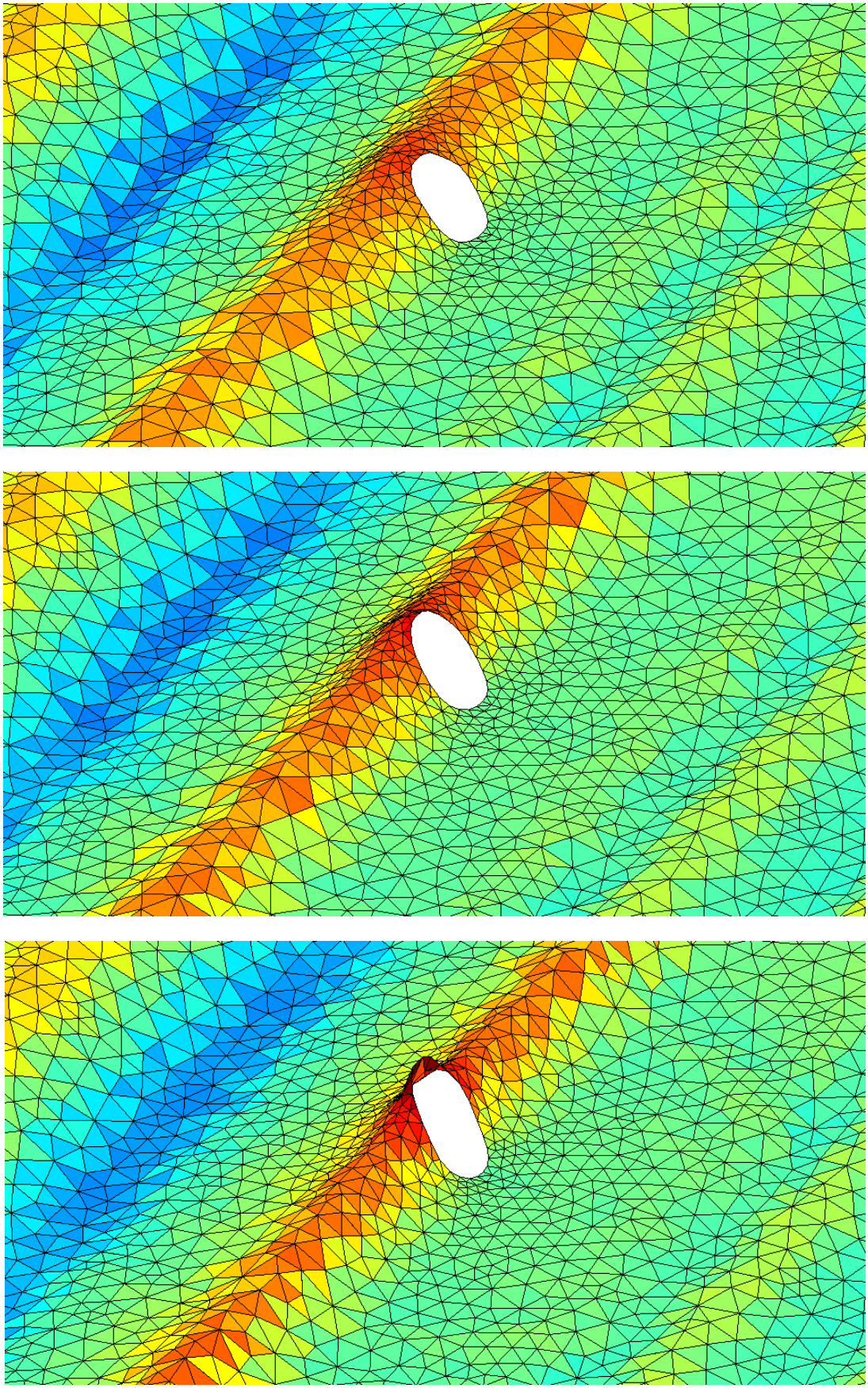

Figure 19: Free-surface elevation around the device at $t/T_e = 17.8$ for $H_s = 2m$ (top), $H_s = 4m$ (middle) and $H_s = 6m$ (bottom).

($H_s = 6m$) than for the smallest sea state ($H_s = 2m$) due to higher order contributions. Such contributions result in a larger and narrow crest and shallower and broader trough on either side of the crest. In terms of wave run-up, it is clear that for the largest sea-state significant run-up occurs on the device – so significant that a finer time-step immediately before and after the interaction is needed to yield a convergent solution.

The total response and power capture time-histories for the $H_s = 2m$ sea state have already been presented as part of Figure 11 but it is useful to show (see Figure 20) the linear and higher order contributions separately for comparison with the more nonlinear simulations. Although small higher order contributions may be present in the time-histories for the odd harmonics and even harmonics of heave response, it is likely that they are negligible and that the first and second order terms are dominant given the weakly nonlinear nature of the incident waves. Therefore, it is more useful to discuss the results in terms of first/linear and second order contributions to velocity and power absorption. This is also applicable to the sea state with twice the significant wave height $H_s = 4m$. In Figure 20 (b) the odd harmonic term which is dominated by the product of the first and second order velocity terms can be positive or negative because the second order velocity term can reduce or increase the total power absorbed. It should be noted that for the power absorbed the even harmonic corresponds to the product of the odd harmonic velocity terms. For example, in Figure 21 the power absorbed by the device from waves generated by the standard wavemaker signal is for some time intervals smaller and other intervals greater than the device power absorption from waves generated by the inverted wavemaker signal. Therefore, the effect of second order velocity terms can be both constructive and destructive for total power absorption. The mean power absorbed over the course of the final $200s$ of the simulation for the waves generated from the unshifted wavemaker signal is $83.4kW$ while it is $82.0kW$ for the wavemaker signal shifted by π (inverted wavemaker signal. The ratio of the contribution of the second order velocity component of power absorbed to the contribution of the first order term is 0.008.

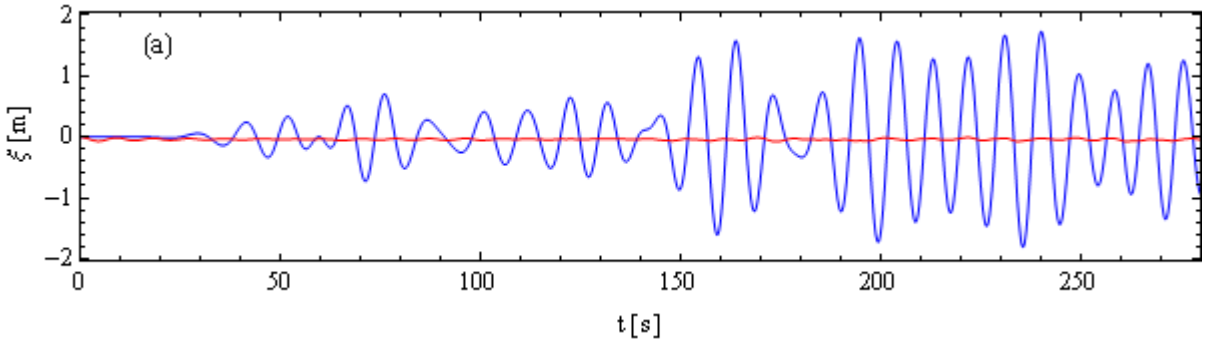

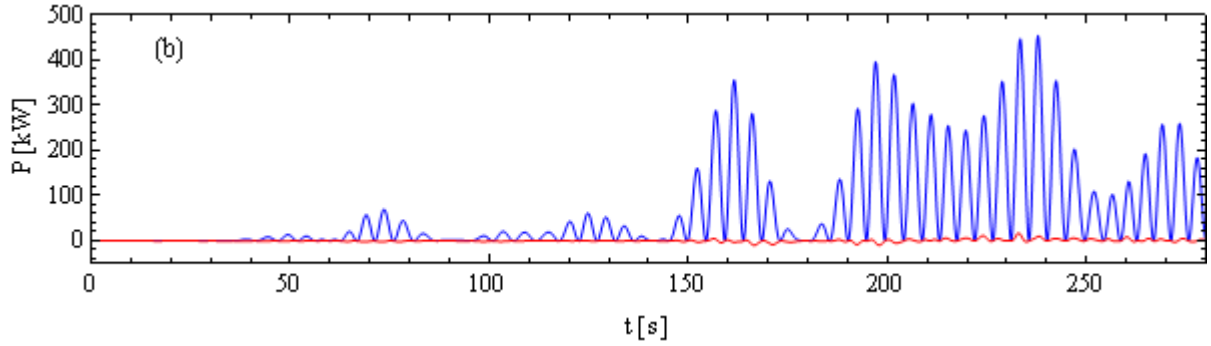

Figure 20: (a) Heave response time history for odd (blue) and even harmonics (red) and (b) the instantaneous power absorbed at even (blue) and odd (red) harmonics for sea state 2 ($H_s = 2m$).

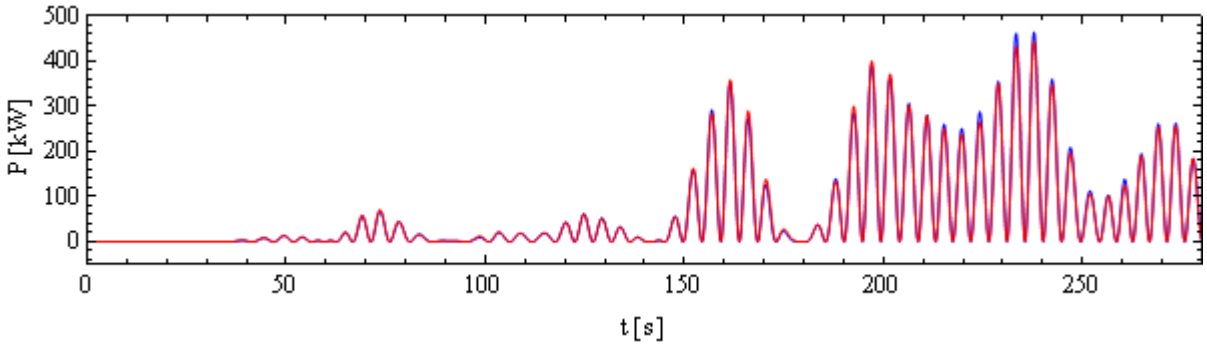

Figure 21: Power absorbed by the device for the irregular sea state SS2 with the wavemaker signal unchanged from that described in section 2.2.1 (blue) and for the inverted wavemaker signal (red).

An increase in the significant wave height from $H_s = 2m$ to $H_s = 4m$ yields more significant second order contributions to device response and power absorption as can be seen by comparing Figure 22 toFigure 20. The mean power absorbed over the final $200s$ of the simulation for the 'crest focussed' irregular waves of significant wave height $H_s = 4m$ is $342.4kW$ while for the 'trough focussed' irregular waves it is $336.6kW$. The ratio of power absorbed solely from first order velocity terms to power absorbed involving second order velocity terms is 0.017 in this case. It is clear that power absorption involving the second order velocity component is becoming relatively more important as the wave height increases. However, in this particular case study where the natural frequency of the device and PTO system is approximately equal to the peak frequency of the incident energy spectrum the contributions of the second order velocity terms to power absorbed is still quite small. If the natural frequency of the device was close to twice the peak incident wave frequency then it might be expected that the second order contributions might excite resonant motions of the device and so second order hydrodynamics might result in significant power absorption contributions. The results of the simulation of power capture for a device in an incident sea state with significant wave $Hs = 6m$ are not presented here because the OXPOT simulation of the interaction for large incident waves and device motions at $t \simeq 200s$ 'broke down' due to a failure of the numerical solution to converge. It is likely that this corresponds physically to the occurrence of wave-breaking and the production of local 'white-water'. The onset of physical wave breaking cannot be modelled by a potential flow code and hence the solution will not converge.

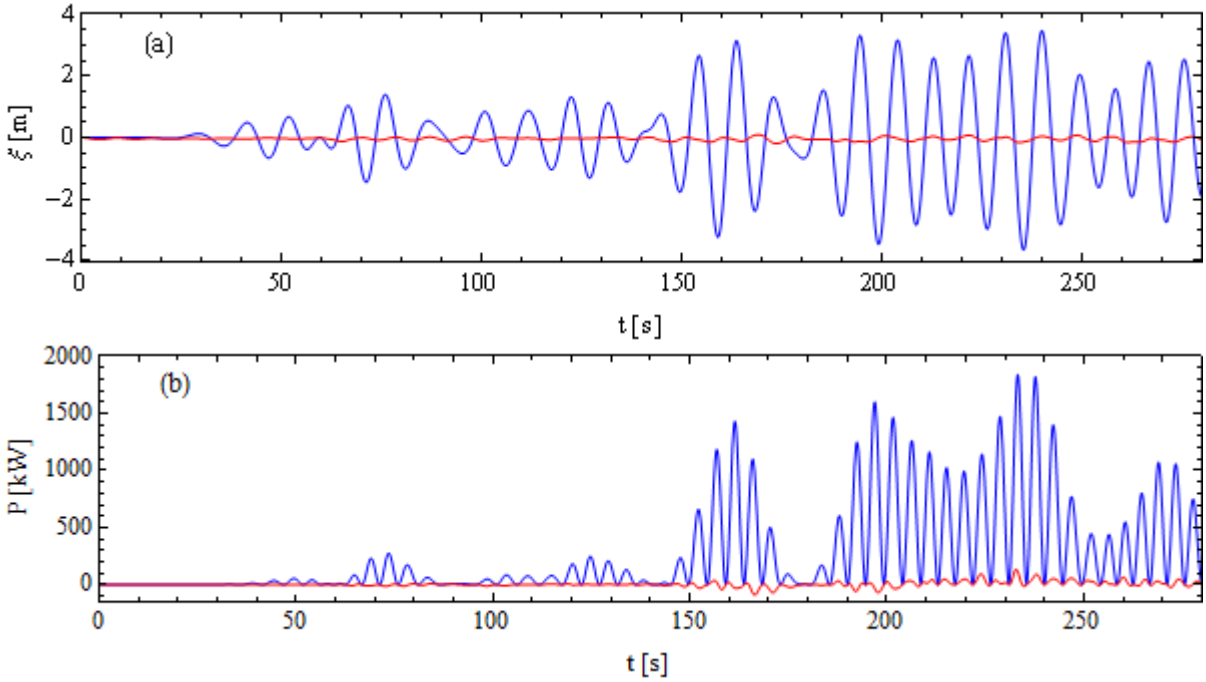

Figure 22: (a) Heave response time history for odd (blue) and even harmonics (red) and (b) the instantaneous power absorbed at even (blue) and odd (red) harmonics for sea state 2 with significant wave height $H_s = 4m$.

4 OPERATION OF SQUARE ARRAYS OF DEVICES IN IRREGULAR WAVES

The performance of an array of four heaving devices in a square configuration is analysed in this section and, where possible, the performance of the front and rear devices compared to that of a device in isolation. The array performance is simulated for all four sea states presented in Table 1 with both linear and nonlinear PTO forces compared for some of the sea-states. Linear PTO forces are simulated for each sea-state in order to provide results for comparison with other numerical methods such as the spectral wave energy converter model (SPECWEC and the spectral solver used by WaveFarmer) and the linear frequency-domain module of (WaveFarmer). The irregular waves generated for the SPECWEC comparison are based on the frequency information for the incident waves used to generate the existing SPECWEC results. Before analysing the results of the OXPOT simulations the array layout and the properties of the boundary meshes used for each sea state are summarised.

4.1 Array configuration and computational domains

A single square array configuration is considered in the following based on the schematic shown in Figure 23. In this particular configuration, four cylinders with rounded ends of radius $a = 0.2h$, where h is the water depth, are positioned with their axes of rotational symmetry at the corners of a square with a side length of three cylinder diameters (corresponding to the case $d = 6a$ in the schematic). Furthermore, the unidirectional sea states have incident wave headings of $\beta = 0$. The inter-device spacing is specified to be relatively small so that significant hydrodynamic coupling may occur between the devices and also to restrict the computational domain size thus preventing the computational times from becoming prohibitively large. The problem of wave reflection at the domain boundary walls can be a significant issue for arrays where the diffracted waves tend to be larger than in the case of a single isolated device. A brief discussion of the particular factors which give rise to more significant reflections and an example of the occurrence of large side-wall reflections is provided later.

The discretisation of the computational domain boundary at the beginning of the OXPOT simulations for the four-body interaction with incident waves from sea state 1 and 3 are shown in Figure 24. By exploiting the symmetry of the interaction problem it is necessary to solve for one half of the total domain only. The computational domain width is half the total domain width; in some cases we will refer to the domain half-width when discussing the computations. The water-wave problem is non-dimensionalised prior to solution so that one unit in the computational domain corresponds to one water depth h. The quadrilateral elements and triangular elements are delineated in this plot but none of the mid-point nodes are shown. Domain decomposition is also clearly evident in these mesh plots and in each case one smaller subdomain is present. For the domain involving sea state 3 simulations the extra subdomain is present to ensure the wavemaker (leftmost wall) is sufficiently far from the array and for the sea state 1 mesh it is to allow a larger damping zone at the right end of the domain while, in both cases, preserving the symmetry of the mesh around the cylinders.

The domain and the mesh element sizes vary significantly for the incident sea states because of the difference in the nature of the sea state spectra. In sea state 1 (SS1), the energy period $T_e = 6.5s$ corresponds to a peak wave period of $T_p \simeq 7.3s$ with a wavelength of $\lambda_p \simeq 1.68h$. In contrast, the energy spectrum of sea state 3 has an energy period $T_e = 11.3s$, corresponding to a peak wave

period of $T_p \simeq 13.1s$, and a peak wavelength of $\lambda_p \simeq 4.68h$. The triangular free-surface elements for the simulation involving sea state 1 are of length $\Delta x = 0.08$ which gives approximately 20 elements per peak wavelength (and hence 10 elements per second order sum bound wavelength). It is worth repeating that each triangular element contains six nodes with a mid-point node on each side of the element so that a large number of elements is not necessary to resolve each wave. The free-surface elements for the SS3 simulations have side lengths of $\Delta x = 0.1875$ which is more than twice that of the elements for SS1; there are approximately 25 per peak incident wavelength. The domain dimensions are also dependent on the peak incident wavelengths. For example, the wavemaker is a distance $7.5h$ or over $1.5\lambda_p$ from the centre of the array for the SS3 simulations while for the SS1 simulations it is $3.6h$ or over $2.0\lambda_p$ from the centre of the array. For the longer waves, evanescent wave generation is not as significant an issue and so it was considered sufficient to place the array less than two wavelengths from the array centre in these (SS3) simulations. Furthermore, the half-width of the domain is $4.0h$ for SS3 and $2.4h$ for SS1 corresponding to approximately 0.8 times the peak wavelength for SS3 and 1.5 times the peak wavelength for SS1, respectively. However, the reflections for the simulations involving sea-state 1 are much more evident than for sea-state 3 (as can be seen later in this section when the results are presented). To explain this it is necessary to consider the properties of the rounded cylinder relative to the incident sea states.

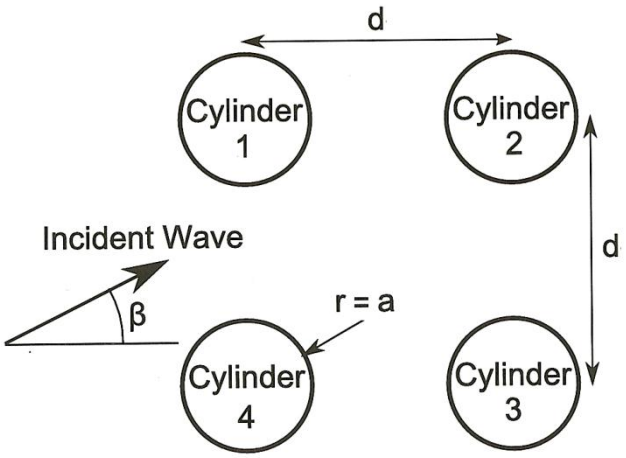

Figure 23: Four device array configuration for cylinders with rounded ends of radius a spaced a distance d apart.

The rounded vertical truncated cylinder has a radius of $0.2h$ and a total draft of $0.4h$ and has a natural resonant period of approximately $9.3s$. Oscillations at this resonant period generate waves of wavelength $2.65h$. The device response is largest when motion excitation involves waves with periods approximately equal to this natural period. The body response for the long period wave motion associated with the peak of spectrum SS3 will be smaller than at resonance – this has been illustrated in the case of the uncontrolled device response to regular waves of period $9.0s$ and $15.0s$ in WG1 WP1 D10. Therefore, it can be expected that the waves radiated by the device for an incident wave with peak spectral period of $T_p \simeq 13.1s$ will not have significant amplitudes and, in particular, the amplitudes of the radiated waves will have spread out and dispersed sufficiently to be of negligible influence on the device motion after reflection. The importance of diffraction can be assessed by considering the non-dimensional parameter ka which measures the device size relative

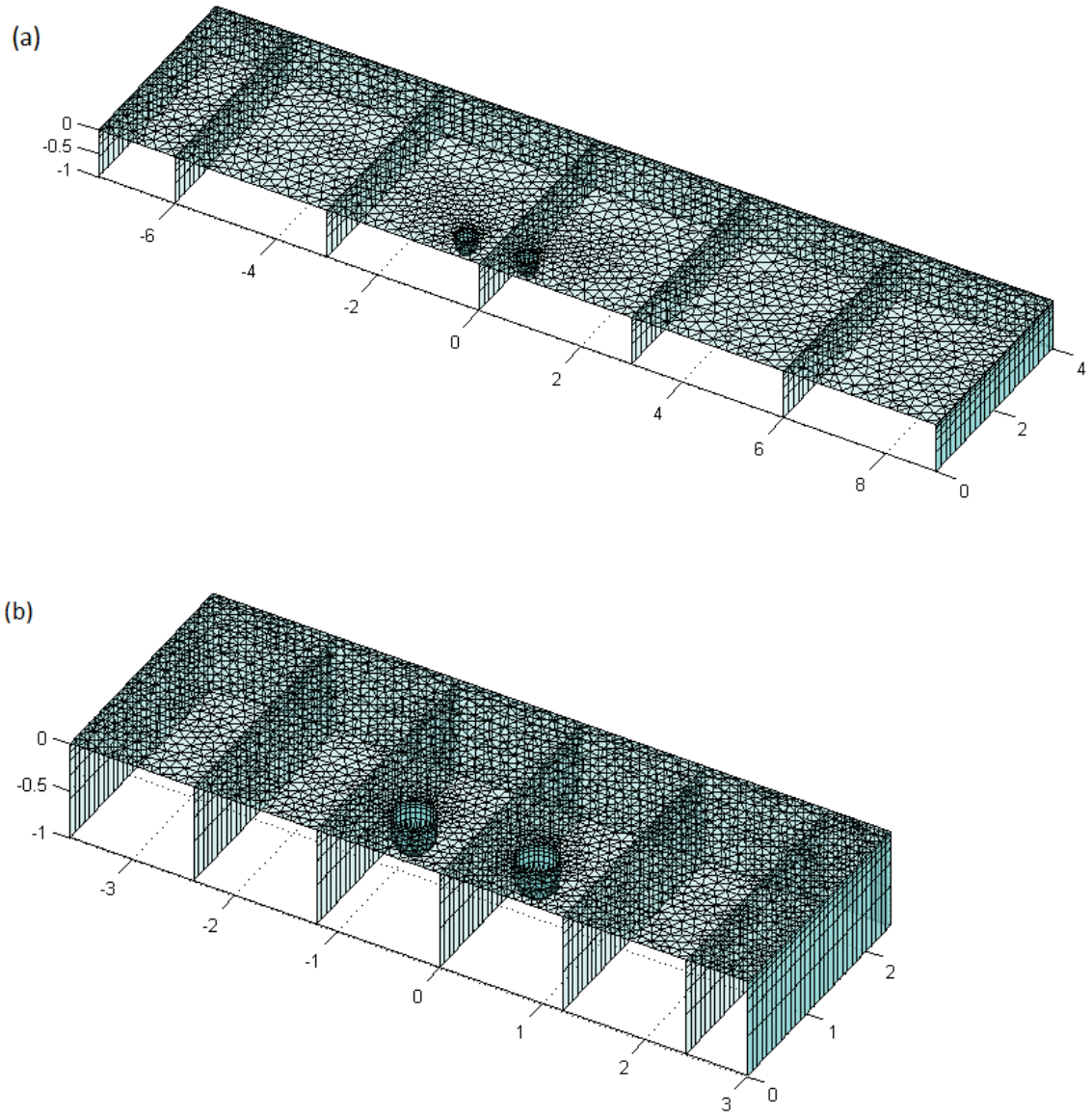

Figure 24: Computational mesh for simulations of the performance of four rounded cylinders in (a) sea state 3 and (b) sea state 1. The computational domain forms only one half of the total domain – the solution is symmetric about the near 'wall' $y = 0$ – so only two structures are plotted.

to the incident wavelength. For incident waves with a period equal to the spectral peak for SS3 the wavenumber parameter ka (where k is the wavenumber) is approximately 0.25 and, for the peak wave period of SS1, the parameter is approximately 0.75. A threefold increase in the wavenumber parameter will correspond to a significant increase in wave diffraction so that the diffracted waves will be significantly larger for an array of devices in sea state 1 compared to an array in sea state 3. As a consequence, it is necessary to create a wider (relative to the peak wavelength) domain for the array in irregular sea state 1 because both diffracted and radiated waves will be larger in relative terms compared to those in sea state 3.

The rounded truncated cylinder is discretised with a finer mesh for interactions in sea state 1 than for sea state 3 because of the significant difference in the peak values of the spectral frequencies. It would be preferable to have a finer discretisation of the mesh in sea state 3 to minimise the

discrepancy between the discretised volume and actual volume of the rounded truncated cylinder, as described in section 3.1. However, the stability of the numerical simulation is reduced by large local variations in the element size particularly on the free-surface. Therefore, the difference between the element length on the open free surface and on the boundary of the free surface (e. g. at the intersection with the body) must be not be too large. A coarser mesh on the body is thus inevitable for waves of longer periods and wavelengths. A summary of the mesh specifications for computational domain boundaries in the simulations of the different sea states is provided inTable 5. In this table the domain half-width and length are abbreviated as W/h and L/h and the number of elements on the rounded truncated cylinders are divided between the number of structured quadrilateral elements on the vertical cylinder section (N_C) and the number of unstructured elements on the hemispherical bottom (N_{HEMI}). A time-step of one-fortieth of an energy period was used for all the array simulations. Depending on the incident irregular waves the simulation times ranged from 25 energy periods to 35 energy periods and thus the simulations consisted of between 1000 and 1400 time steps.

Sea state – (T_e, H_s)	λ_p/h	**Domain**		**Body elements**		**Total**	
		L/h	W/h	N_C	N_{HEMI}	**Element**	**Nodes**
SS1 – $(6.5s, 2m)$	1.67	6.6	2.4	(28×5)	226	7882	21320
SS2 – $(8.0s, 2m)$	2.64	12.0	3.25	(20×5)	218	7980	21282
SS3/4 – $(11.3s, 2m/3m)$	4.68	16.5	4.0	(16×5)	164	6870	18522

Table 5: Summary of the computational mesh specifications for the domain boundary in OXPOT simulations involving the operation of rounded end cylinders in sea states 1 – 4.

4.2 Simulations of array operation using SPECWEC frequency discretisation

In the first set of simulations of the performance of an array of four truncated cylinders with rounded ends in irregular seas the incident wave-field was specified based on a set of discrete frequencies provided by QUB for the spectral model work. This set of frequencies, prescribed for sea state 3, consists of 26 values ranging from $f = 0.04Hz$ to $f = 0.5Hz$ and the frequency increment is not constant but increases with increasing values of the frequency. In this case, the amplitude of each wave component is weighted to give more energy to the sea state depending on the size of the frequency increment. This clear from equation (6) where the wave amplitude depends on $S(f)\Delta f$ which is the area of the integral 'strip' under the spectral function after discretisation by a given set of frequencies. A plot of the spectrum for sea state 3 is shown in Figure 25. A random set of phases was generated for the wave components, whose amplitudes were determined from equation (6), to give a particular realisation of sea state 3. The linear free-surface elevation at the origin (corresponding to the centre of the array) is plotted in Figure 26 for this realisation. In the OXPOT simulations it takes approximately $90s$ for the waves to arrive at the array when wave-generation begins from time $t = 0$ at the wavemaker a distance $7.5h$ from the centre of the array. Therefore, only the last $200s$ of the simulation, i.e. the time interval $(110s, 310s)$, yields acceptable power absorption results and the mean power absorbed is computed over that time interval. A relatively short time interval of 20s is allowed for the device motion to be excited before measuring the power absorption. However, the waves at peak frequency arrive before $t = 90s$ (the higher frequency, lower energy waves arrive slightly later than the peak waves) so some motion is excited from $t = 70s$ as shown in Figure 27.

The array performance over 27.5 energy periods in the realisation of sea state 3 corresponding to Figure 26 was simulated and the response and power absorption of the pair of front and rear devices in the array are plotted in Figure 27. In the array schematic shown in Figure 23 the front devices are indexed 1 and 4 and the rear devices are indexed as 2 and 3. In the OXPOT simulations only the

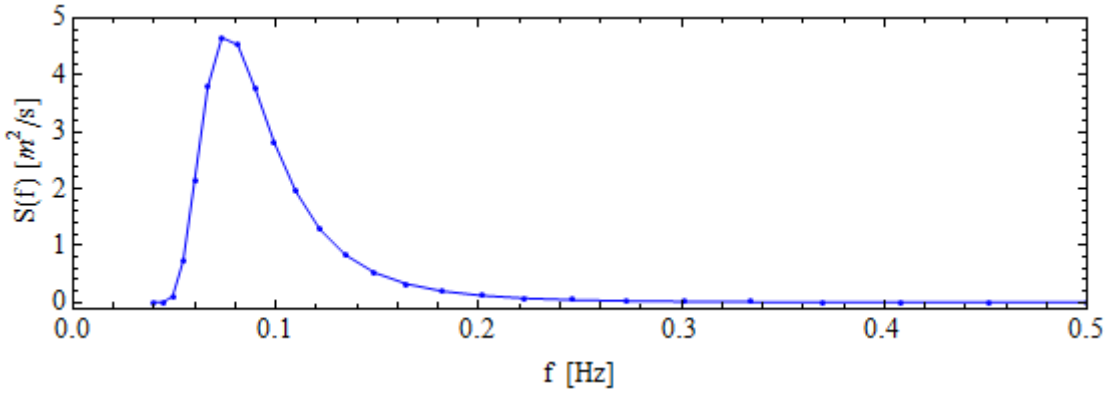

Figure 25: Discretised spectrum for sea-state 3 using frequencies prescribed by QUB.

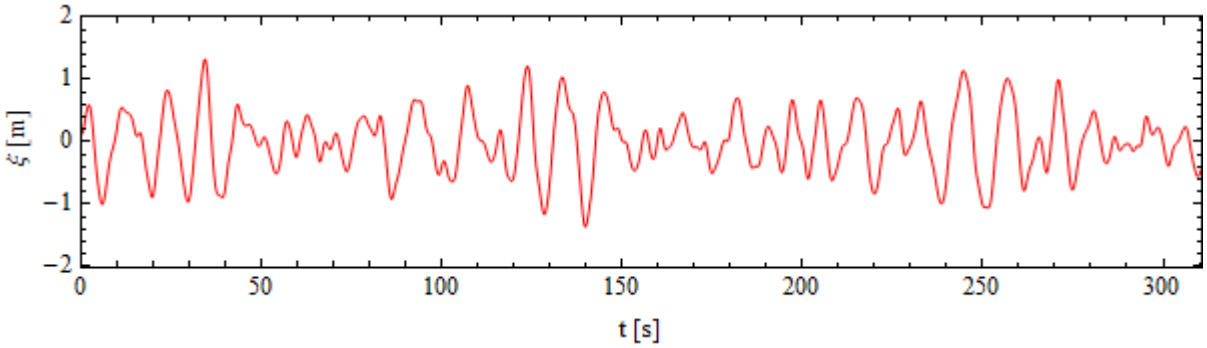

Figure 26: Linear free-surface elevation for a realisation of sea state 3 based on the discretised spectrum in Figure 25.

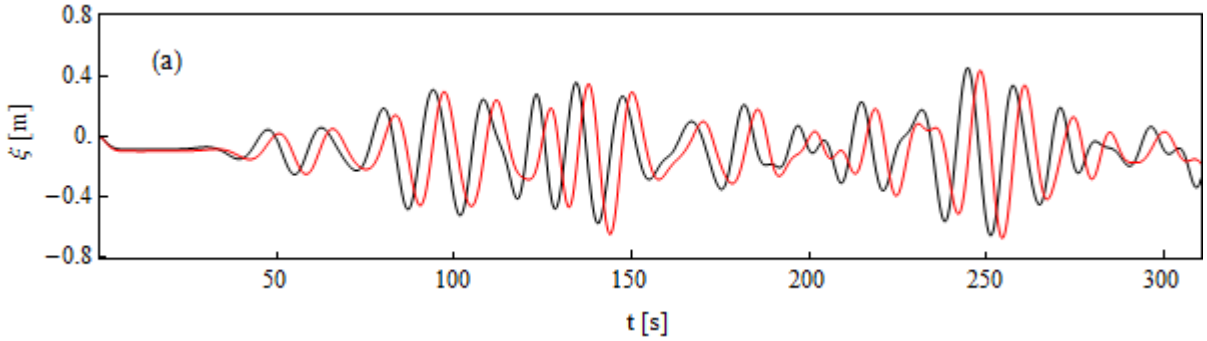

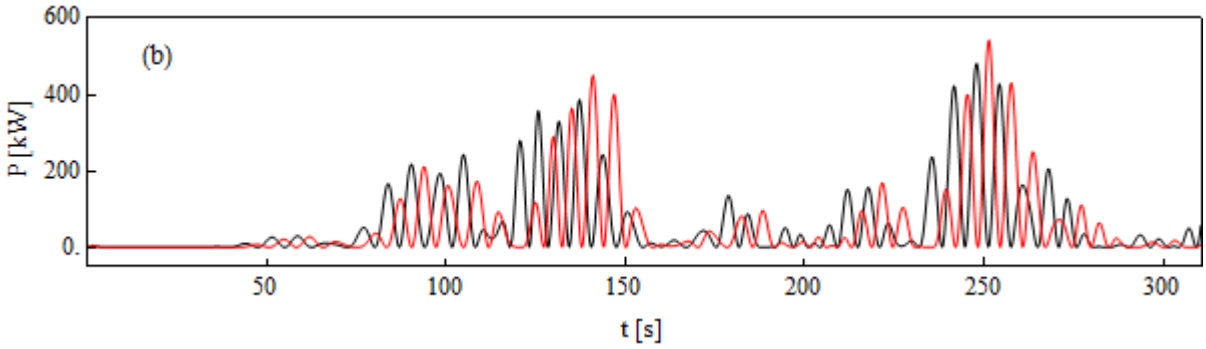

Figure 27: (a) Heave response and (b) instantaneous power capture time-histories of the front (black) and rear (red) device in the square four-body array in a realisation of sea state 3.

motion of devices 1 and 2 are simulated – the symmetry of the interaction problem means that devices 4 and 3 move identically to devices 1 and 2, respectively. It is worth noting that the largest response and power capture intervals for the device occur at the times of largest wave incidence at the centre of the array, i.e. just before $t = 150s$ and at $t = 250s$. Any large waves occurring prior to $t = 90s$ will not have arrived at the array in the OXPOT simulation due to a delay in wave propagation from wavemaker which begins generating at $t = 0s$. The mean power absorbed is computed on the interval $(95.8s,\ 310.5s)$ which corresponds to the final 19 energy periods of the simulation. For the front device the mean power absorbed is computed to be $75.8kW$ while for the rear device it is computed to be $70.3kW$.

In this simulation, the mean power capture is not obtained over a full repeat period because this would result in unfeasibly large computational times. Therefore, the wave energy incident on the devices may not equal the target incident wave energy specified by the spectrum. As a consequence, the significant wave height of the sea state over the interval upon which the mean power is computed may not equal the target significant wave height $H_s = 2m$. Therefore, in an attempt to obtain an approximation to the mean power absorbed over a full repeat period the mean value measured in the simulation P_M^S is scaled as follows

$$P_M = P_M^S (H_s^L / H_s)^2 \tag{24}$$

where H_s^L has been computed from the linear incident wave data at the centre of the array over the interval on which the instantaneous power absorbed is averaged. In brief, this scaling expression is an attempt to adjust the averaged value to take into account the difference between the target incident wave energy and the wave energy incident on the array over the averaging interval. In this case, the mean power absorbed by the front devices and rear devices is $79.1kW$ and $73.3kW$, respectively. However, it is not done as standard and is merely an attempt to obtain the best estimate for mean power capture results given the simulation length and the actual sea state period. In the next section, results are presented for simulations with durations that are sufficiently long to include response information for a complete sea-state repeat period.

The operation of the device in sea state SS4 was also simulated. In the case of the experimental investigations sea state 4 corresponds to an energy period and significant wave height of $(T_e, H_s) =$

$(11.3s, 3m)$. The simulation duration in this case is $25T_e$ and the incident waves were generated by scaling the wave amplitudes c_n so that $H_s = 3m$ and maintaining the same phases. The power absorption time-history for the front and rear array devices is shown in Figure 28 and it follows the same trends as for the incident sea state SS3. The device responses and power absorption results in sea state 3 were scaled by H_{SS4}/H_{SS3} and $(H_{SS4}/H_{SS3})^2$, respectively, and compared to the correspond sea state 4 results to investigate any nonlinearity effects. However, the sea-states are quite linear and no visible difference is observed when plotting and comparing the time-histories. The mean power absorbed is computed over the interval $(95.8s, 282.5s)$ and, after it is adjusted using (24) and the measured significant wave height at the origin ($H_s = 3.104$m), then we obtain $P_M = 183.1kW$ for the front device and $P_M = 167.9kW$ for the rear device. It is important to remark that if the interval over which the power absorbed is relatively short then, even after adjusting for the discrepancy in the measured and target incident wave energy, there will be some variations in the measured power absorbed depending on the particular sea state realisation considered. In general, the mean power absorbed becomes more reliable the longer the averaging interval.

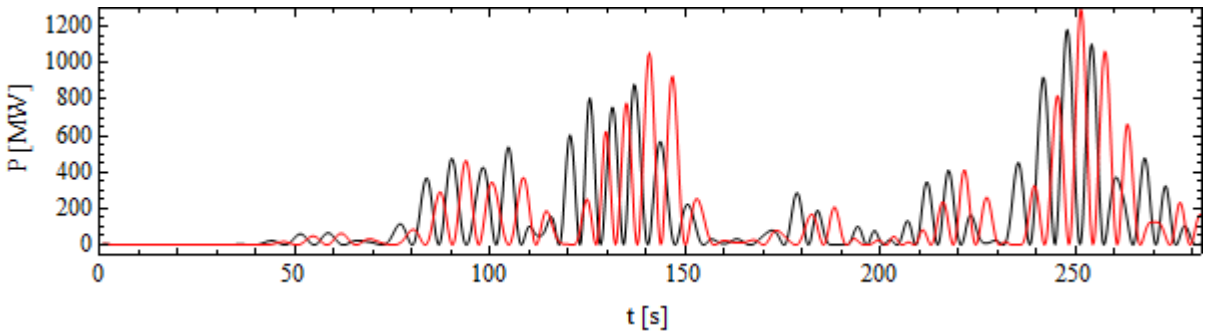

Figure 28: Instantaneous power capture time-histories of the front (black) and rear (red) device in the square four-body array in the same realisation of sea state 3 as before but for a significant wave height $H_s = 3m$.

4.3 Simulations of array operation using alternative spectral frequency discretisation

In order to obtain a more reliable estimate of the average power absorbed from a given sea state (and to avoid scaling the mean power using measured and target significant wave heights) a different set of frequencies to those prescribed for the spectral wave model computations were used. The frequency increment was chosen to correspond to a pre-determined repeat period in the same manner as described for realisations of sea state 1 and 2 in section 2.2.1. In order to prevent computational times becoming prohibitively large it was decided to choose a repeat period of $200s$. Therefore, the value of the frequency increment was equal to $0.005Hz$ and the wave amplitudes for the sea state were then obtained on the interval $(8f, 80f) = (0.04Hz, 0.4Hz)$ at each frequency increment. The same discretisation was used for the energy spectrum of sea-state 2 and the spectral discretisation is illustrated in Figure 2. It should be noted that a repeat period of $200s$ corresponds to almost 18 energy periods for SS3 and 25 energy periods for sea state 2.

Two simulations of array performance in this realisation of sea state 3 have been conducted – one with a linear PTO force with a damping coefficient $c_{PTO} = 7.0 \times 10^6 Nm/s$ and the other with Coulomb damping PTO force with a comparable amplitude to the linear case. No restoring force coefficient was introduced because an investigation into the effect of the PTO restoring force has already been conducted for the case of a single isolated body. The mean power absorbed by the linear PTO will be compared with the result from the last section to ensure some consistency and to assess the effect of using equation (24) to improve the power absorption estimate. A Coulomb damping force amplitude comparable to the linear PTO damping force was computed using equation (14) for the motion of device 1 subject to the linear PTO force. The heave responses of the device subject to the linear and nonlinear PTO forces are compared in Figure 29. The response of the devices is larger when subject to the Coulomb damping PTO force during periods of significant motion excitation. However, when successive waves incident on the device subject to the Coulomb damping PTO force have relatively small amplitudes the motion response is minimal (e.g. during the time interval $(150s, 190s)$ for device 1). This is consistent with the single body analysis of the Coulomb damping force.

The instantaneous power absorbed for the front and rear devices in the square array are shown in Figure 30 for the linear and nonlinear (Coulomb) damping PTO forces. The mean power capture values are presented in the third and fourth entry of Table 6 which summarises all the array power capture results. The time-histories for the devices subject to the respective PTOs are quite similar – the peaks in the power absorbed have similar amplitudes with only a slight time-lag in the time at which they occur. Upon closer inspection of the time histories over a short time interval (Figure 31) it can be seen that the peaks for the Coulomb PTO force are wider than those for the linear PTO force. Therefore, it is not surprising that when the mean power absorbed is computed over the final $200s$ of the simulation that the values for the Coulomb PTO force ($94.4kW$ for the front device and $89.2kW$ for the rear device) are significantly larger than for the linear PTO force ($76.2kW$ for the front device and $69.2kW$ for the rear device). In terms of the linear PTO force, it is clear expression (24) to adjust the mean power absorbed when the mean is not taken over a full repeat period has not been effective. The mean power absorbed before adjustment was $75.8kW$ and $70.3kW$ for the front and rear devices respectively. After the adjustment for the measured incident wave spectrum the mean power was computed to be $79.1kW$ and $73.3kW$ for the front and rear device, respectively, as shown in the first entry in Table 6. Based on this analysis, to obtain a good mean power absorption estimate it is necessary to specify a repeat period of reasonable length for the computation.

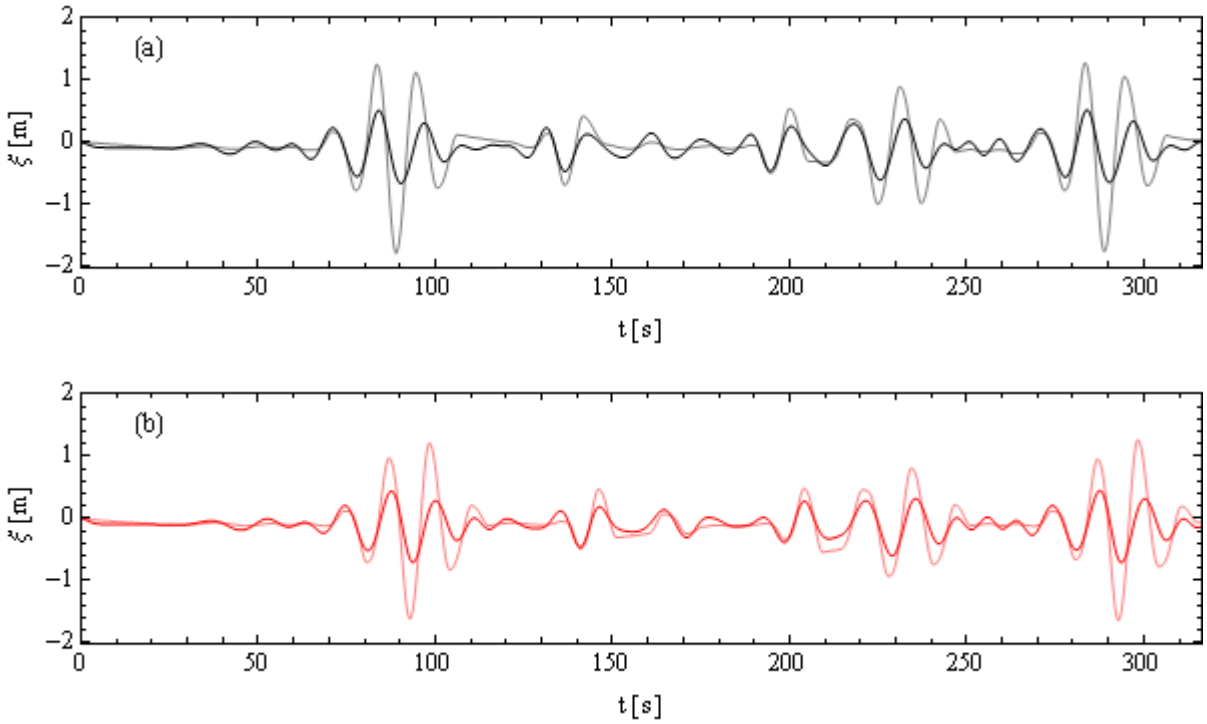

Figure 29: Heave displacement time-history of (a) the front device and (b) the rear device subject to a linear PTO force (black, red) and subject to a Coulomb damping force (grey, pink) in sea state 3.

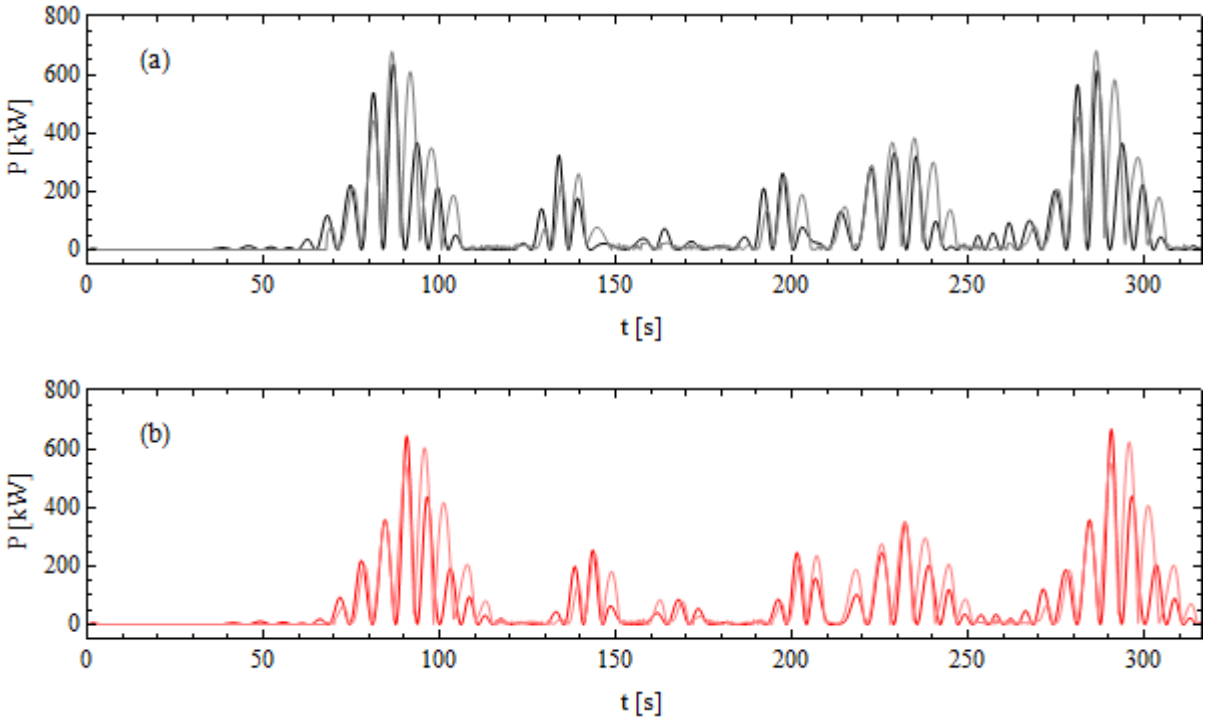

Figure 30: Power absorption time-history of (a) the front device and (b) the rear device subject to a linear PTO force (black, red) and subject to a Coulomb damping force (grey, pink) in sea state 3.

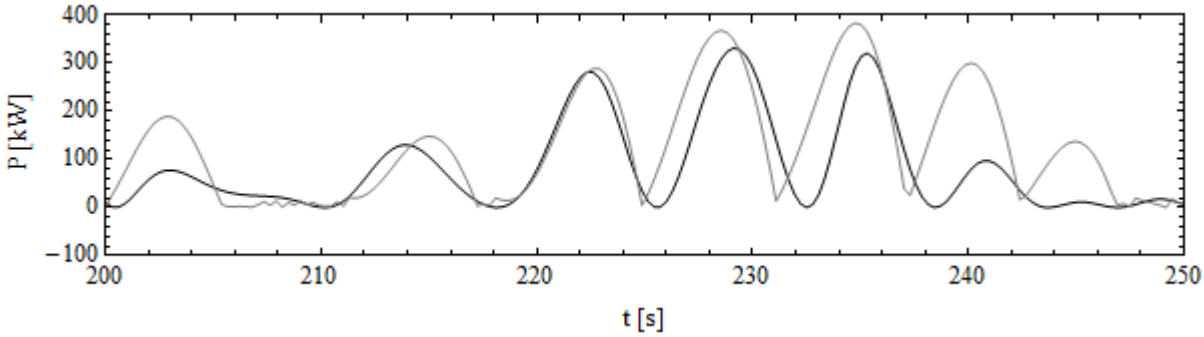

Figure 31: Comparison of the shape of the power absorption peaks for the front device in the square array responding to excitation from irregular sea state 3 subject to the linear PTO force (black) and the nonlinear (Coulomb) PTO force (grey).

The array performance for irregular waves generated from the spectrum for sea state 2 ($T_e = 8.0s$ and $H_s = 2m$) was also simulated and the results are presented in the fifth entry of Table 6. Irregular wave generation was achieved using the same amplitudes and phases as were used in the single isolated device analysis described in section 3.3. The distance from the wavemaker of the single isolated device and the front device in the square array was chosen to coincide so that the effect of the surrounding devices on array performance could be assessed in a straightforward manner. The linear PTO damping coefficient specified by QUB (referred to as the 'strong' damping case in section 3.3) was used in the simulation. Before comparing the motion and power capture of the device at the front of the array to the single isolated device, the response and power capture of the front and rear array devices are shown (see Figure 32). It is worth noting that the repeat period of $200s$ for the incident wave should correspond not only to a repeat in the incident free-surface elevation signal every $200s$ but also a repeat in the displacement and power absorption time-histories for the device, provided the transient wave front of the incident wave generated at the wavemaker has passed. However, comparing the response of device 1 in Figure 32 (a) just after time $t = 50s$ and after time $t = 250s$ it is clear that, although similar, the responses are not identical. It can thus be concluded that all the frequency components of the incident irregular sea have not fully arrived at the array at time $t = 50s$ – in particular the high frequency components travel slower than the low frequency components and take longer to arrive. This is in contrast to the response and power absorption time-histories shown in Figure 29 and Figure 30 for the array performance in sea state 3 where a clear repeat of the peak in response and power absorption is visible at around $90s$ and $290s$. A longer simulation of the sea state 2 interaction would yield a full repeat period of response and power capture without the effect of the transient start-up.

The comparison of the device response and power capture for a device at the front of the array and the single isolated device is shown in Figure 33. The front device was chosen because it was located at the same distance from the wavemaker as the isolated device and hence the time-histories were directly comparable. More significant differences will exist for comparisons between the isolated device and rear array device. The device velocity rather than displacement are compared because the discretisation errors in the array simulation and single device simulation are slightly different due different body element specifications (the single device simulation only requires the discretisation of half the body due to symmetry) and so the equilibrium displacements are slightly offset due to discretised volume differences. Differences in the velocity time histories are relatively small implying that device interactions are minimal. The device interactions due to wave radiation are likely to be

negligible due to the small response amplitudes of the devices and so only the diffracted waves affect the device motion in the array. The mean power absorbed by the front

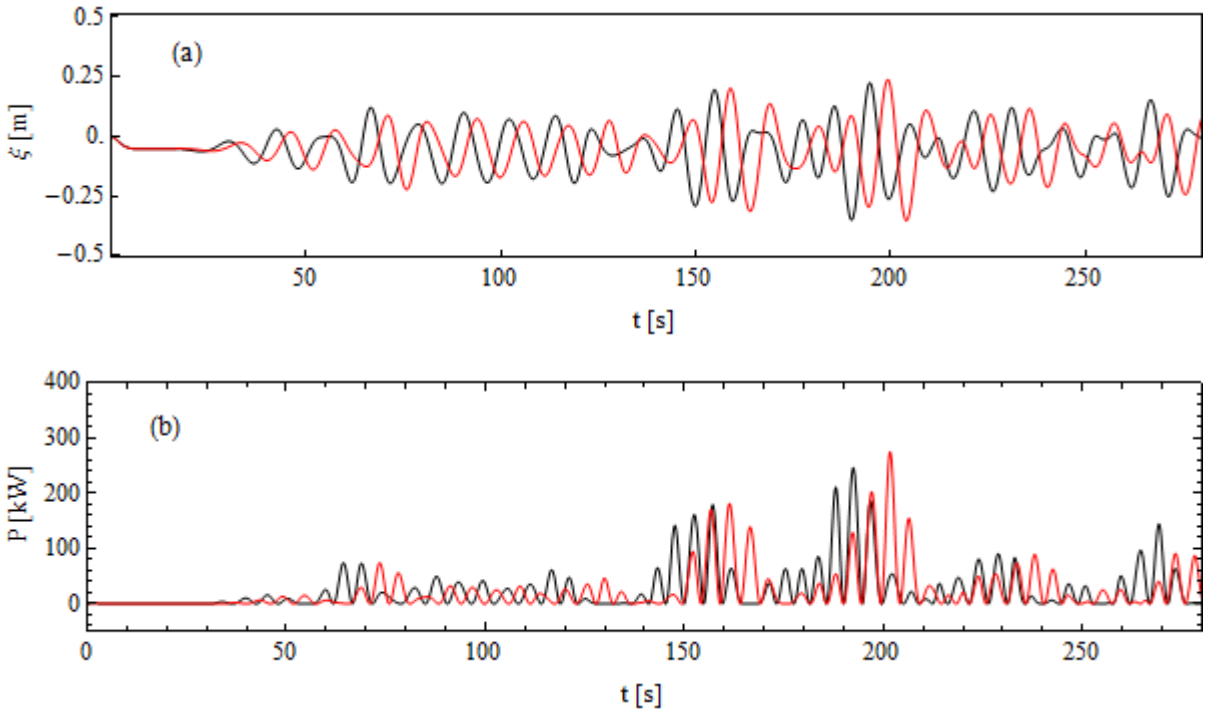

Figure 32: (a) Heave displacement and (b) instantaneous power capture time-histories of the front (black) and rear (red) device in the square four-body array in a realisation of sea state 2.

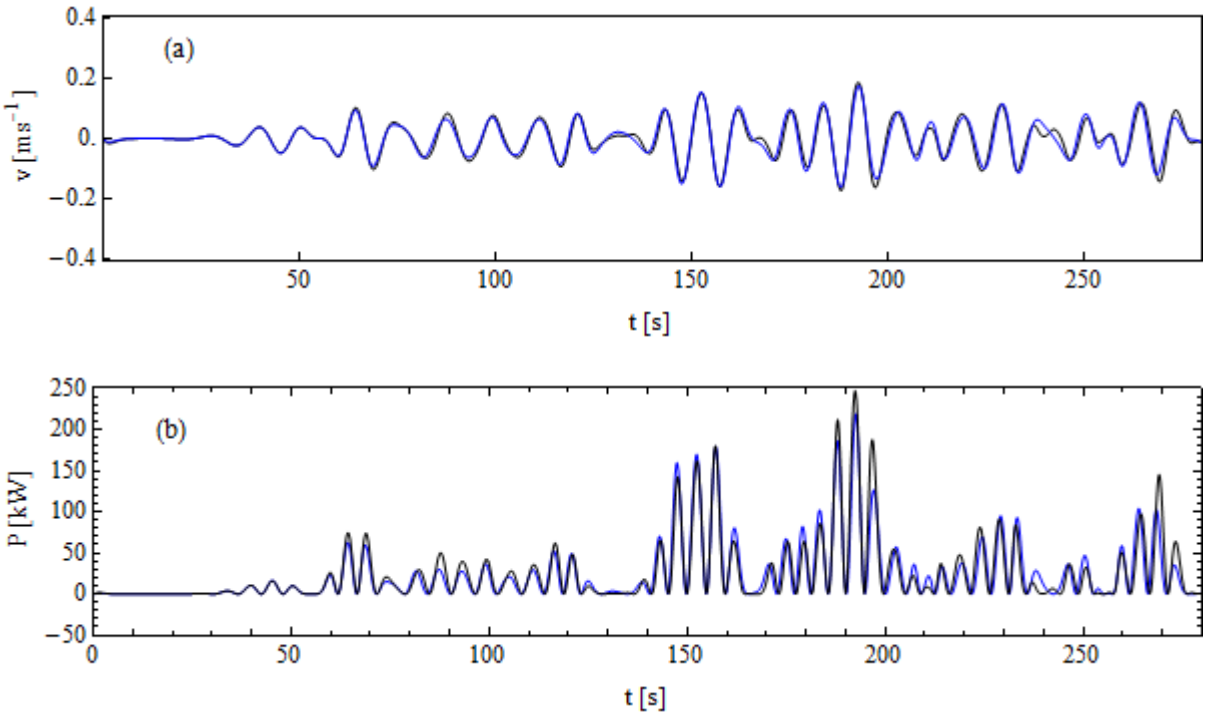

Figure 33: (a) Heave velocity and (b) instantaneous power capture time-histories of the front device in the square array (black) and a single isolated device (blue) in a realisation of sea state 2.

and rear devices in the array over the last $200s$ of the simulation is $32.1kW$ and $30.1kW$ respectively and this compares to $31.5kW$ for the single isolated device. Therefore, interaction effects are minimal in this case but are very slightly favourable in terms of performance for the device at the front of the array and unfavourable for the device at the rear of the array.

To complete the set of array performance simulations and to provide more results for comparison with WaveFarmer the operation of the array of four devices in sea state 1 and sea state 4 was simulated. The linear PTO coefficient values were chosen to equal those specified in WaveDyn results provided by GH for the complete set of experimental sea states including the subset of unidirectional sea states listed in Table 1. The results for sea state 4 are presented next. However, it is first important to note that the target energy spectrum for waves generated in the OXPOT and WaveDyn simulations have peak periods of $11.3s$ but significant wave heights of $H_s = 4m$ for the former and $H_s = 3m$ for the latter. Nevertheless, the mean power absorbed can be adjusted for this difference in significant wave height using the same adjustment as expressed in equation (24) assuming the nonlinearity of the sea states is negligible. The incident irregular waves were generated with a new set of wave amplitudes and phases and not by scaling the SS3 wave amplitudes to yield a significant wave height of $H_s = 4m$. However, the repeat period of the waves was chosen to be $200s$ once again. The linear PTO damping coefficient was specified to have value $2.2399 \times 10^5 Nm^{-1}s$. Displacement and power capture time-histories for the response and power capture for the front and rear devices in the array are shown in Figure 34. The mean power capture over the last $200s$ of the simulation for the devices at the front of the array was $187.2kW$ and for the devices at the rear of the array it was $172.3kW$. Assuming the contribution to the instantaneous power absorbed from higher order nonlinear terms is negligible, the mean power absorbed can be adjusted by the factor $(3/4)^2$ to obtain the power absorbed by the devices in the equivalent sea state with a significant wave height $H_s = 3m$. This adjustment yields a mean power capture value of $105.3kW$ for the device at the front of the array and $96.9\ kW$ for the device at the rear of the array.

The WaveDyn simulation, using an irregular incident wave field comprising over 1000 wave components at frequency increments of $df \simeq 0.00044$ corresponding to a repeat period of approximately $2720s$, yielded mean power capture values of $112.5kW$ and $107.0kW$ for the devices in the sea state with peak period $11.3s$ and significant wave height $3m$. The difference between the WaveDyn and the OXPOT results can be ascribed to a number of different factors:

- the irregular waves generated by OXPOT do not have as many frequency components present and if the peak of the spectrum is not resolved correctly some energy may not be accounted for;
- the length of the repeat period in the OXPOT simulations is relatively short compared to the WaveDyn simulation;
- the scattered and radiated OXPOT waves, even if small, will be reflected and influence the response of the device – a small change in the response velocity can lead to larger changes in the power due the quadratic dependence on velocity.

A more detailed comparison of the OXPOT and WaveDyn results would require the generation of the same irregular wave field in OXPOT as is specified in WaveDyn followed by the analysis of the response of the device subject to a prescribed PTO. Given that the power absorbed is derived from

the velocity of the device a more accurate assessment of the difference in the numerical methods could be obtained from comparing the response velocity time-histories from both methods.

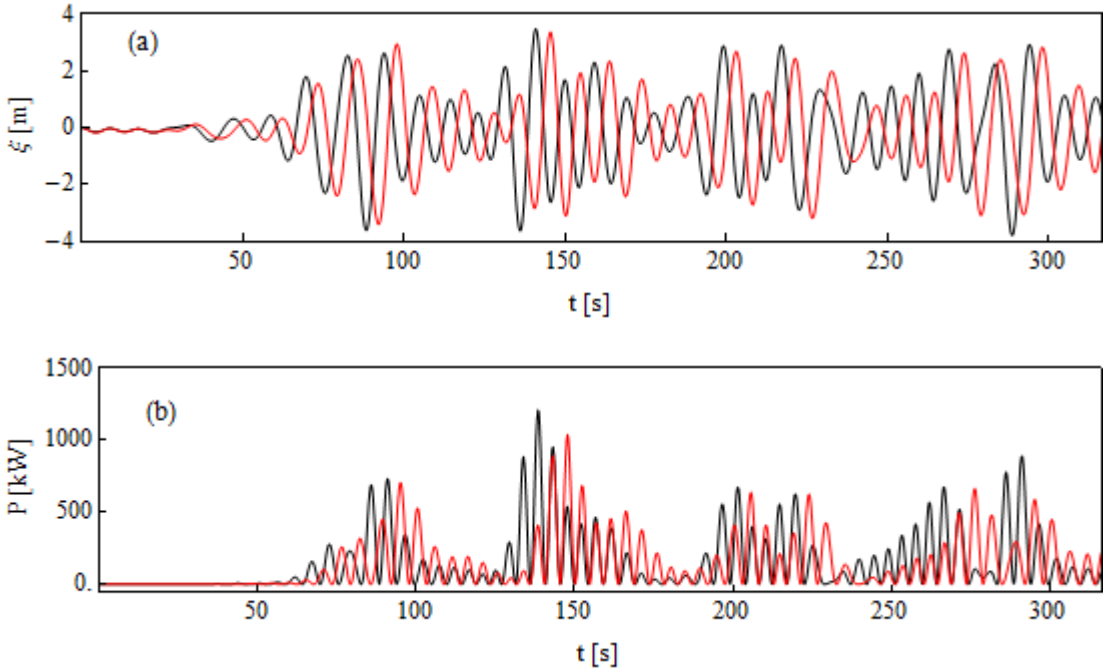

Figure 34: (a) Heave displacement and (b) instantaneous power capture time-histories of the front (black) and rear (red) device in the square four-body array in a realisation of sea state 4.

The final array interaction simulation for an array of devices in sea state 1 utilises the spectral discretisation described in section 2.2 and the domain boundary discretisation as presented in Table 5. Therefore, the repeat period of the simulation is $160s$ and the half-width of the domain is $2.4h$ which corresponds to a distance of $1.6h$ between the side wall and the array devices. As stated previously, the interaction parameter for the peak frequency of sea state 1 is $k_p a \simeq 0.75$, where $k_p = 2\pi/\lambda_p$, and so the scattered waves are expected to be significant during the interaction. For significant wave scattering, a domain with a distance of less than one peak wavelength ($\lambda_p = 1.68h$) between the devices and the side wall is quite narrow. An analysis of the heave displacement and power absorption time histories, shown in Figure 35, suggests that the reflected waves may play a significant role in the dynamics of the device after $t \simeq 140$ because very little randomness is evident in the behaviour. A quasi-resonant build-up of the heave displacement amplitudes occurs over the last $60s$ of the simulations. Furthermore, a plot of the free-surface after 28 energy periods shows the presence of scattered/radiated waves throughout the domain including near the wavemaker. Here, the wave-front is no longer uniform but varies perpendicular to the direction of wave incidence indicating the presence of interfering scattered/radiated waves. Furthermore, to the sides of the array there are some complex free-surface variations corresponding to interference between outgoing, reflected and incident waves. As noted previously, the importance of artificial reflections on body dynamics depends both on the domain width and on the relative amplitudes of the radiated or scattered waves to the amplitude of the incident waves.

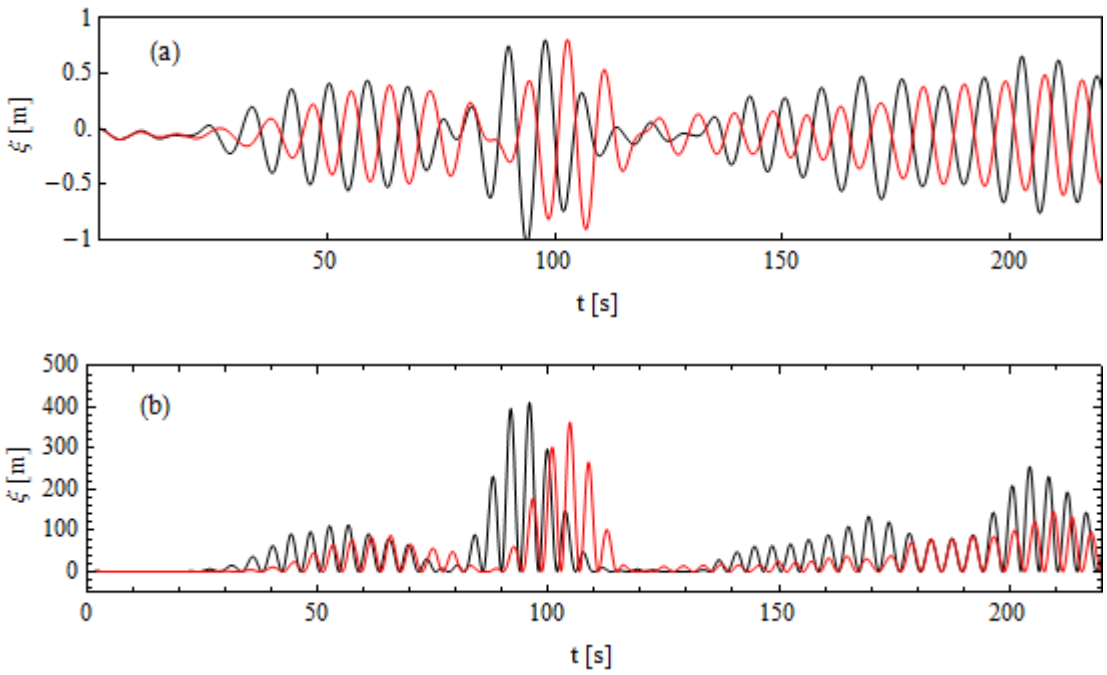

Figure 35: a) Heave displacement and (b) instantaneous power capture time-histories of the front (black) and rear (red) device in the square four-body array in a realisation of sea state 1.

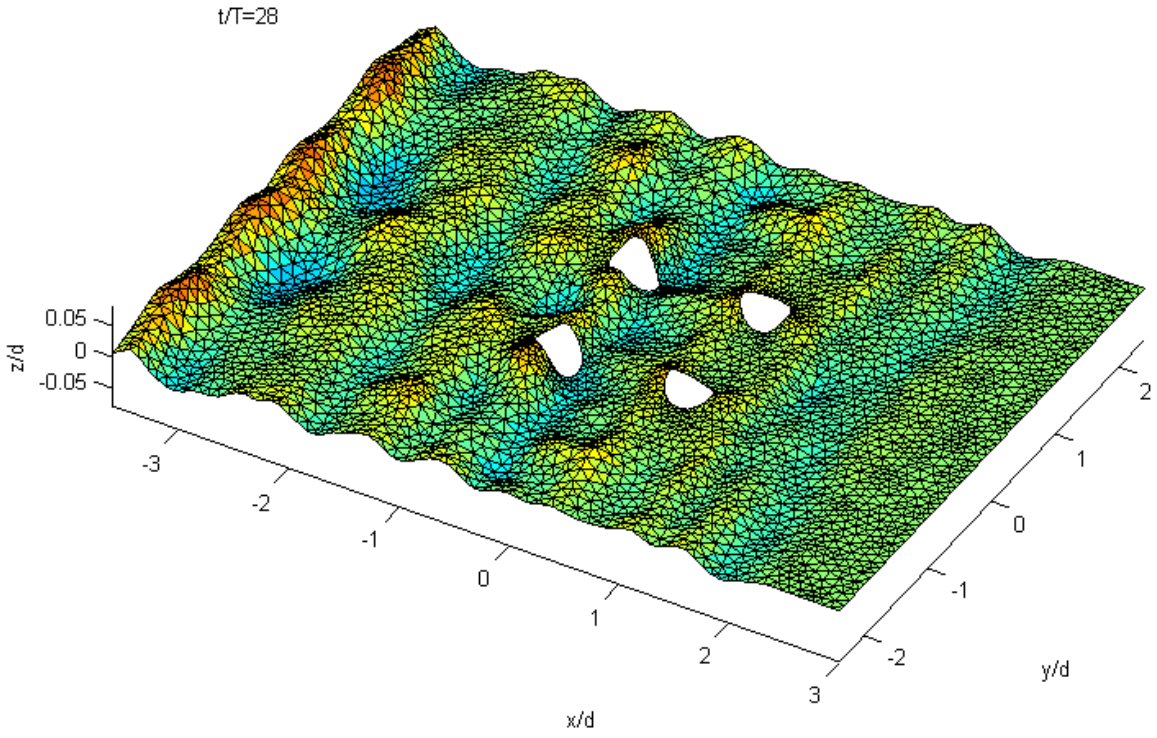

Figure 36: Free-surface elevation throughout the computational domain for the interaction between the array and incident irregular waves from sea state 1.

The mean power capture results from the simulations of the performance of the devices in the square array in each sea state are summarised in Table 6. If the frequencies of the wave components of a given realisation of a sea state correspond to the spectral discretisation specified by QUB then this realisation is denoted 'QUB'. Otherwise, if the sea state has been realised with a set of wave components specified here (so that the simulation includes a full repeat period of reponse and power absorption data) then the realisation is denoted 'OX'. The final entry for $SS4$ has $H_s = 4m$ specified because the previous entry for SS4 uses $H_s = 3m$. There is an ambiguity about what value H_s should take for SS4 – for experiments $H_s = 4m$ led to local wave breaking and so the significant wave height was reduced to $H_s = 3m$. The 'Averaging Interval' column contains the length of the interval over which the mean power absorbed is computed for each simulation. In the PTO column the linear damping coefficient or Coulomb damping amplitude is presented for each simulation and the power capture results are provided separately for the front and rear devices in the square array. The percentage decrease in the mean power capture from the front device to the rear device is also provided. In all simulations, the observed decrease is quite small in all cases at less than 10%. This can be attributed to the fact that the peak wavelengths in each of these simulations are large relative to the device size and device motions are small so that much of the incident wave energy is transmitted past the front row of the device. Therefore, most of the incident wave energy is available to the rear devices also. The smallest peak incident wavelength occurs in sea state 1 and it is expected that the percentage decrease in power capture may be larger in this case due to an increase in wave energy scattering at the front row of the array.

Sea state	Realisation	Averaging Interval	PTO	Mean Power Capture		
			Linear/ Nonlinear	Front $[kW]$	Rear $[kW]$	% decrease rear-to-front
SS3	QUB	$(95.8s, 310.5s)$	$7.0 \times 10^6 Nm^{-1}s$	79.1	73.3	7.3%
SS4	QUB	$(95.8s, 282.5s)$	$7.0 \times 10^6 Nm^{-1}s$	183.1	167.9	8.3%
SS3	OX	$(116.4s, 316.4s)$	$7.0 \times 10^6 Nm^{-1}s$	76.2	69.2	9.2%
SS3	OX	$(116.4s, 316.4s)$	$7.40 \times 10^5 N$	94.4	89.2	5.5%
SS2	OX	$(80s\ , 280s)$	$7.0 \times 10^6\ Nm^{-1}s$	32.1	30.1	6.2%
SS4	$H_s = 4m$	$(116.4s, 316.4s)$	$2.24 \times 10^6\ Nm^{-1}s$	187.2	172.3	8.0%

Table 6: A summary of the mean power capture results for the OXPOT array simulations.

4.4 Note on computational times

The array simulations were very computationally intensive as they involved more than 1000 time-steps for a BEM solution of a system with from 18,000 to 21,000 nodes (see Table 5). On a single desktop computer with an quad-core Intel Xeon processor of clock speed 2.93GHz and $6GB$ of memory per core the simulation of the array interaction in sea state 2 (1400 time-steps) took approximately 190hrs. The OXPOT executable in this simulation included OpenMP parallelisation of the matrix assembly and matrix solution routines. Clearly, the scope for longer simulation times and larger domains is limited. However, using the Oxford Supercomputing Centre (OSC) clusters it was possible to reduce the computational times to somewhat more reasonable levels. The simulation of the array operation in sea state 1 which involved 1200 time-steps required a computational of time 70 hours on a single node of the latest OSC cluster. The improvement in computational speed is mainly due to the increase in the number of cores available (16) per computing node. For this

simulation the OpenMP parallelisation yielded almost a six-fold decrease in computational time compared to a single-threaded (single CPU) computation. Nevertheless, the best benchmark for the computational times is for the desktop PC as it does not incur any overheads. However, if required significantly shorter computational times can be achieved.

5 CONCLUSIONS

The results of fully nonlinear simulations for the performance of a single axisymmetric device, a long line of devices and a square array of four devices in irregular waves are presented in this report. The geometry of the axisymmetric device is that of a rounded vertical truncated cylinder (more specifically it is vertical cylinder with a hemispherical end) which is consistent with the geometry of the device used by QUB in the experimental investigations. Both linear and nonlinear PTO forces were considered – the nonlinear PTO force is a Coulomb damping force – and the effect of phase control through the PTO restoring force was also investigated. A brief investigation into the importance of nonlinearity is also presented here.

To obtain estimates of average power capture for devices in irregular seas it is first necessary to implement wave generation which yields irregular waves with mean properties such as significant wave height and the peak or energy period which are consistent with the target spectrum. Furthermore, some degree of random of randomness must also be incorporated in the wave generation. It was considered sufficient to use deterministic wave amplitudes (based on the target spectrum) and random wave phases to form the set of wave components which constitute the random sea. Although some of the randomness of real waves is lost with this method, the mean properties of the waves are consistent with the target spectrum and so the mean power absorption values obtained from these irregular wave simulations should be reliable.

In a previous deliverable (WG1 WP1 D10) the improvement in power absorption through the application of optimal power absorption conditions for linear PTO damping and restoring force coefficients in regular waves was demonstrated. Thus, it was decided to investigate the suitability of applying these regular wave optimal power conditions to an irregular wave interaction involving a

spread of incident wave frequencies. The sea states considered were unidirectional with spectra which were JONSWAP in shape with a maximum γ value of 2 and so were not particularly narrow-banded. Nevertheless, by choosing the PTO damping coefficient to optimise power capture at the peak incident wave frequency an improvement in the mean power absorption of a single isolated device compared to that with a substantially different PTO coefficient was observed in sea state 2. In particular, the PTO damping coefficient optimised for the peak spectral frequency was more than an order of magnitude less than the value specified by QUB in the SPECWEC computations. – hence in the discussion that followed the optimal damping coefficient for the peak frequency was referred to as the 'weakly damped' interaction and the other damping coefficient as the 'strongly damped' interaction. An improvement of more than a factor of two in the mean power absorption (in the same incident irregular waves) for the device with 'weak' PTO damping compared to the strongly damped case was observed.

To further investigate the applicability of the regular wave optimal PTO coefficient relations (15) and (18) to power capture in irregular waves, a moderate PTO restoring force coefficient was specified and the power absorbed during the same irregular wave incident was computed and compared to the equivalent case with no PTO restoring force. In sea state 2, where the peak spectral period $(T_p = 9.3s)$ was approximately equal to the natural resonant period of the device, the introduction of a PTO restoring force modified the resonant frequency of the system and the net result was a change in the resonant period of the device-PTO system from $9.0s$ to $8.6s$. A reduction in the mean power capture of approximately 15% from $83.4kW$ to $70.2kW$ was observed due to addition of the PTO restoring force. Therefore, it is concluded that the optimal linear PTO relations are still relevant to the power absorption performance of devices in irregular seas. It is likely that small changes in the PTO coefficient values do not yield as significant differences in mean power capture as for regular waves but the optimal values certainly provided useful guidelines for optimising power capture. Furthermore, the resonant frequency of the system plays a significant role in power capture – improvements in power absorption can be achieved by ensuring the resonant frequency and peak spectral frequency are similar.

To fully realise the capabilities of OXPOT as a fully nonlinear potential flow solver, simulations of moderately nonlinear events must be conducted. However, the sea states used in the experimental tests, and which have been modelled using linear solvers, are all very weakly nonlinear. In order to observe the effects of nonlinear hydrodynamics (as opposed to the effects of nonlinear power take-off) it was therefore necessary to increase the significant wave height of the sea states to introduce small-to-moderate second order contributions to the incident irregular sea. For the experimental sea state SS2 $(T_e = 8.0s, H_s = 2m)$ the nonlinearity parameter $\varepsilon = H_s/\lambda_p$ was approximately equal to 0.02 or equivalently $k_p A_s = 0.063$, where $\lambda_p$is the peak wavelength of the spectrum, $k_p = 2\pi/\lambda_p$ is the peak wavenumber and the amplitude term is defined as $A_s = H_s/2$. In the realisation of sea state 2 implemented in the simulations described in section 2 the nonlinear contribution to the free-surface elevation was negligible, and similarly for device response to the incident wave excitation and instantaneous power absorbed from the incident waves. Doubling the significant wave height $(\varepsilon = 0.04)$ led to moderate second-order contributions to the free-surface elevation – the presence of nonlinear contributions to the free-surface was particularly evident for a large event occurring in the vicinity of the structures. Small second order contributions were also present in the fully nonlinear response of the device and in the device power absorption. Finally, a sea state with a

significant wave height three times greater than the original sea state 2 was also investigated. Clear second-order structure was evident in the free-surface elevation during a large wave event and the response of the device also included larger second order contributions than previously observed. However, the largest events were close to wave breaking and in this case OXPOT, as a potential flow solver, is limited in its ability to simulate such interactions. In this case, however, where the second-order sum incident wave frequency was much higher than the natural frequency of the device, the response at second order and the associated power capture were relatively small compared to the linear contributions. Tuning the device to have a natural frequency close to the peak incident wave frequency is quite standard and the probability of the second order sum frequency and the natural device frequency having similar values in practice is low.

In the array simulations presented here, the power absorption of the front and rear devices in a square array were computed for the unidirectional experimental sea states. The device spacing was specified to be 3 diameters and the power capture of the devices subject to both linear and Coulomb damping was computed. For the sea states with peak wave components of relatively long wavelengths, the presence of the other devices had a relatively small effect on the motion of a given device compared to the effect of incident waves. That is, the radiated and diffracted wave-fields were significantly smaller than the ambient incident wave field for the sea states with long peak periods. Similar behaviour was evident in the simulations of the long line of devices at a spacing of three and five diameters, although for this intermediate sea state ($T_e = 8.0s$) there was clear evidence of the influence of surrounding devices on the device motion. For sea state 1 with the shortest wave period, the scattered waves were quite significant relative to the incident waves but due to side-wall reflections it was not possible to assess the importance of the device interactions in this case. For the deliverable D14, where comparisons between OXPOT and WaveDyn simulations will be made, it may be possible to extend the domain and reduce the importance of wave reflections.

In the next deliverable, it will be necessary to simulate some of the experimental tests conducted by QUB and reported in WG2 WP2 D5. In its current state of development, OXPOT is capable of simulating all of the single device and four device array tests involving regular waves, irregular waves and focussed wave groups. However, with the large computational times reported in section 4.4 for these relatively short irregular wave tests it will be practically very difficult to simulate long intervals of the irregular wave tests. Given that the sea states are very weakly nonlinear this would in any case be an unwise allocation of computational resources. Instead, the simulation of the focussed wave group tests which will involve moderate nonlinearity will take precedence. The regular wave tests will also be considered and possibly some of the larger wave/response events which arise in the irregular sea tests. The implementation of a Coulomb damping force with a value representative of the actual Coulomb damping force applied to the device in the experiments is just one aspect of the simulation of experimental tests that will prove challenging. Nevertheless, given that OXPOT is capable of modelling, among other things, Coulomb damping PTO forces, irregular wave interactions and focussed wave group interactions, it should be possible to simulate much of the physics of the experimental interactions.

REFERENCES

Bai, W. & Eatock Taylor, R., 2006. Higher-order boundary element simulation of fully nonlinear wave radiation by oscillatiing vertical cylinders. *Applied Ocean Research,* Volume 28, pp. 247-265.

Mavrakos, S. A. & McIver, P., 1998. Comparison of methods for computing hydrodynamic characteristics of arrays of wave power devices. *Applied Ocean Research,* Volume 19, pp. 283-291.

Tucker, M. J., Challenor, P. G. & Carter, D. J. T., 1984. Numerical simulation of a random sea: a common error and its effect upon wave group statistics. *Applied Ocean Research,* 6(2), pp. 119-122.